Spatiotemporal variations of wetland backscatter: The role of water depth and vegetation characteristics in Sentinel-1 dual-polarization SAR observations

Boya Zhang [a,*], Shimon Wdowinski [a], Daniel Gann [b], Sang-Hoon Hong [c], Jay Sah [d]

[a] *Institute of Environment, Department of Earth and Environment, Florida International University, Miami, FL 33199, USA*
[b] *Institute of Environment, Department of Biological Sciences, Florida International University, Miami, FL 33199, USA*
[c] *Department of Geological Sciences, Pusan National University, Busan 46241, South Korea*
[d] *Institute of Environment, Florida International University, Miami, FL 33199, USA*

ARTICLE INFO

ABSTRACT

Synthetic Aperture Radar (SAR) backscatter observations are sensitive to hydrologic conditions and vegetation characteristics of land cover. This study conducted a high spatial-resolution investigation (30-m) on the response of dual-polarization C-band (5.6 cm wavelength) SAR backscatter coefficients ($\sigma°$) to temporal changes of surface water depth (d_w) and spatial variations of vegetation characteristics in the south Florida Everglades wetlands. We investigated (1) linear relationships between $\sigma°$ and d_w values, and (2) the effects of vegetation density and morphology on $\sigma°$-d_w relationships. We developed a new method to classify pixels with significant linear relationships of multi-temporal $\sigma°$ and d_w ($R^2 > 0.5$ and *p*-value <0.04), which were termed "Reliable Scatterer" (RS). RS included positive, negative, and a combination of both positive and negative relationships (corresponding to RS^+, RS^-, $RS^\pm$, respectively). Our analysis revealed spatially varying vegetation densities and morphologies had a significant impact on RS types, where we found RS^+ type pixels for woody vegetation, $RS^\pm$ for a mix of medium- and high-density herbaceous vegetation using C-band VV (C-VV) data, and RS^- for sparse herbaceous vegetation using C-VH data. Overall, our study indicates that C-band dual-polarization backscatter is sensitive to water-depth variations for some vegetation types, and this sensitivity has the potential to serve as a reliable indicator for monitoring water depth in wetland environments.

1. Introduction

Space-based synthetic aperture radar (SAR) observations have provided information for monitoring a variety of land cover types, including wetlands (Kasischke and Bourgeau-Chavez, 1997), agriculture (Le Toan et al., 1997), and polar ice sheets (Goldstein et al., 1993). Consistent monitoring is achieved because the microwave energy employed by SARs can be transmitted through clouds. In addition, SAR acquires observations at all weather and illumination conditions (day and night) with a short revisit time depending on the sensor (e.g., 12 days for Sentinel-1). For wetland ecosystems, such as the southern Florida Everglades, SAR backscatter observations are sensitive to water depths, vegetation characteristics (density and morphology), and soil moisture (especially for non-woody vegetation) (Kasischke et al., 2003, 2009;

Bourgeau-Chavez et al., 2005; J.-W. Kim et al., 2014). Spatiotemporal variations of SAR observations are attributed to the interactions between microwave energy, water surfaces, vegetation (Brisco, 2015), and the SAR acquisition parameters (e.g., wavelength, polarization, and incidence angle) (J.-W. Kim et al., 2014; Lang et al., 2008).

Because microwave energy can be transmitted through vegetation canopies, in dense vegetation, the variations in SAR backscatter are more sensitive to differences in wetland inundation than surface reflection measured by optical remote sensing systems. Backscatter coefficients, or sigma nought ($\sigma°$), defined as the normalized measure of the radar return (per unit area) from a target on the ground, have been successfully used to detect and monitor inundation extent in wetlands with both herbaceous and woody vegetation (Ramsey, 1995; Kasischke and Bourgeau-Chavez, 1997; Pulvirenti et al., 2011, 2013; Brisco et al.,

2013; Brisco, 2015; Tsyganskaya et al., 2018; Zhang et al., 2018; Grimaldi et al., 2020). Methods to detect inundation extent differ between herbaceous and woody vegetation because of different microwave energy-water-vegetation interactions (i.e., scattering mechanisms; Brisco, 2015).

Previous studies showed that radar backscatter coefficients are significantly correlated with changes in water depth (d_w, the distance between the water surface and ground level) with different types of linear relationships according to vegetation types (see Section 2.2) (Kasischke et al., 2003, 2009; Lang and Kasischke, 2008; Puri et al., 2011; Yuan et al., 2015). However, all linear $\sigma°$-d_w relationships in previous SAR studies were based on co-polarized (VV: vertical transmit and vertical receive or HH: horizontal transmit and horizontal receive) observations. To our knowledge, no significant $\sigma°$-d_w relationships have been detected with cross-polarized (VH or HV) observations. For example, previous use of SIR-C cross-polarized observations in marsh sites did not explore backscatter in response to changes in water depths because of the limitation in temporal coverage of the data (Pope et al., 1997).

The interaction of microwave energy with wetlands characterized by diverse and heterogeneous vegetation cover often results in significant spatial variability in backscatter. As hydrological measurements in wetlands were spatially limited to a finite number of stage stations or narrow tracks along altimetry satellite orbits, the linear $\sigma°$-d_w relationships detected previously (Kasischke et al., 2003; Yuan et al., 2015) reflected the microwave energy-water-vegetation interaction only at hydrological measurement points. Expanding the investigation of $\sigma°$-d_w relationships according to vegetation types to the full spatial extent of a wetland requires maps of vegetation cover and water depth at high spatial resolutions compatible with the resolution of SAR data.

This study conducted a high spatial-resolution investigation of dual-polarization, C-band SAR backscatter response to temporal changes of water depth in wetlands with heterogeneous vegetation types. We focused on two study areas located in the Florida Everglades, where daily water-surface data, digital terrain models (DTMs), and high-resolution (2 m) vegetation maps were available. The hydrologic and vegetation data combined with 66 dual-polarized Sentinel-1 scenes that were acquired nearly every 12 days over three years (2016–2019) enabled us to investigate the relationships between multi-temporal $\sigma°$ (C-VV and C-VH) and d_w values for each 30 m × 30 m pixel in the two study areas. We also investigated the effects of vegetation density and morphology on the backscatter's sensitivity to water depth variations by comparing the linear $\sigma°$-d_w relationships for various vegetation types. The linear $\sigma°$-d_w relationships were explained by changes in scattering mechanisms in response to water depth changes relative to vegetation characteristics. This study achieved a better understanding of microwave energy-water-vegetation interactions in wetlands and demonstrated that backscatter data combined with vegetation information has great potential to monitor wetland hydrological conditions.

2. Background

This section provides basic knowledge of microwave scattering from wetlands vegetation. Since this study only uses C-band wavelength SAR data from the Sentinel-1 satellite, we emphasize C-band microwave scattering. Section 2.1 provides the scattering sources from woody and herbaceous vegetation, and Section 2.2 summarizes previous studies that found significant $\sigma°$-d_w linear relationships in wetlands.

2.1. Microwave scattering characteristics of wetlands

The total SAR backscatter coefficient from wetland ecosystems can be modeled by a summation of different scattering sources for woody and herbaceous vegetation types (Kasischke and Bourgeau-Chavez, 1997). For wetlands with shrubs and trees, three layers in the vertical dimension are considered: (1) canopy layer consisting of small branches

and foliage; (2) trunk layer consisting of large branches and trunks or boles; and (3) ground surface layer (Fig. 1). The total backscatter coefficient from woody vegetation, $\sigma°_{t-w}$, can be expressed after Wang et al. (1994, 1995); Dobson et al. (1995); and Kasischke and Bourgeau-Chavez (1997) as:

$$\sigma^0_{t-w} = \sigma^0_c + \tau^2_c \tau^2_t \left(\sigma^0_m + \sigma^0_t \sigma^0_s + \sigma^0_d \right) \tag{1}$$

where

σ^0_c is the backscatter coefficient of the crown layer of smaller woody branches and foliage,

τ_c is the transmission coefficient of the canopy layer,

τ_t is the transmission coefficient of the trunk layer,

σ^0_m is multiple-path scattering between the ground and canopy layer,

σ^0_t is direct scattering from the tree trunks,

σ^0_s is direct scattering from the ground, and

σ^0_d is double-bounce scattering between the trunks and ground.

For herbaceous wetlands, the scattering sources only include the canopy and ground surface layers (trunk layer is removed). The total backscatter coefficient, σ^0_{t-h}, can be simplified to.

$$\sigma^0_{t-h} = \sigma^0_c + \tau^2_c \left(\sigma^0_s + \sigma^0_m \right) \tag{2}$$

Total SAR backscatter is governed by the interaction between the transmitted microwave energy and woody and herbaceous vegetation layers. Canopy and trunk layers are direct sources of scattering of microwave energy (σ^0_c and σ^0_t). However, they also absorb or attenuate microwave energy (Kasischke and Bourgeau-Chavez, 1997), especially for short-wavelength energy (e.g., X- or C-band), resulting in lower transmission than longer wavelengths (e.g., L-band). When the microwave energy employed by SARs is transmitted through the canopy and trunk layers, diffuse scattering occurs from rough surfaces of the ground substrate under the unflooded state (σ^0_s, Fig. 1). Diffuse scattering of the energy results in multiple directions, with a portion returning to the SAR (Fig. 1), and this backscatter is influenced by variations in soil moisture (Kasischke and Bourgeau-Chavez, 1997; Kasischke et al., 2003, 2007, 2009). Under the flooded state without wind, ground surface scattering is eliminated, and all of the microwave energy is forward scattered (specular reflection) from water surfaces. As water depth increases, a higher degree of microwave energy can be transmitted to water surfaces because of less attenuation from woody trunk layers or herbaceous canopy layers. For forests, enhanced ground-trunk (σ^0_d) and ground-canopy (σ^0_m) scattering occurs, whereas, for short herbaceous vegetation, canopy and ground-canopy scattering decrease (Kasischke and Bourgeau-Chavez, 1997; Townsend, 2001, 2002; Kasischke et al., 2003; Lang and Kasischke, 2008).

Double-bounce and multiple-path scattering contribute differently to co- and cross-polarized SAR data. When forested wetlands are flooded, double-bounce scattering increases (Lang and Kasischke, 2008), which is assumed to only contribute to co-polarized backscatter because of little or no depolarization (Fung and Ulaby, 1983; Brisco, 2015). However, Hong and Wdowinski (2014) found that the cross-polarized observations from flooded forests include a double-bounce component induced by rotated ground-trunk dihedrals. Multiple-path scattering involves two bounce scattering that increases both co- and cross-polarized backscatter.

C-band microwave energy interaction with a woody or herbaceous vegetation is associated with biophysical characteristics. For woody vegetation, tree density and canopy closure (leaf-on or leaf-off) determine the degree of energy's transmission through canopies and the sensitivity of backscatter to subcanopy flooded states and soil moisture. During leaf-off periods, more energy is transmitted through canopy layers with higher sensitivity backscatter than leaf-on periods (Townsend, 2001; Lang and Kasischke, 2008; Lang et al., 2008). In addition, forests with larger basal areas and greater heights to the bottom of the
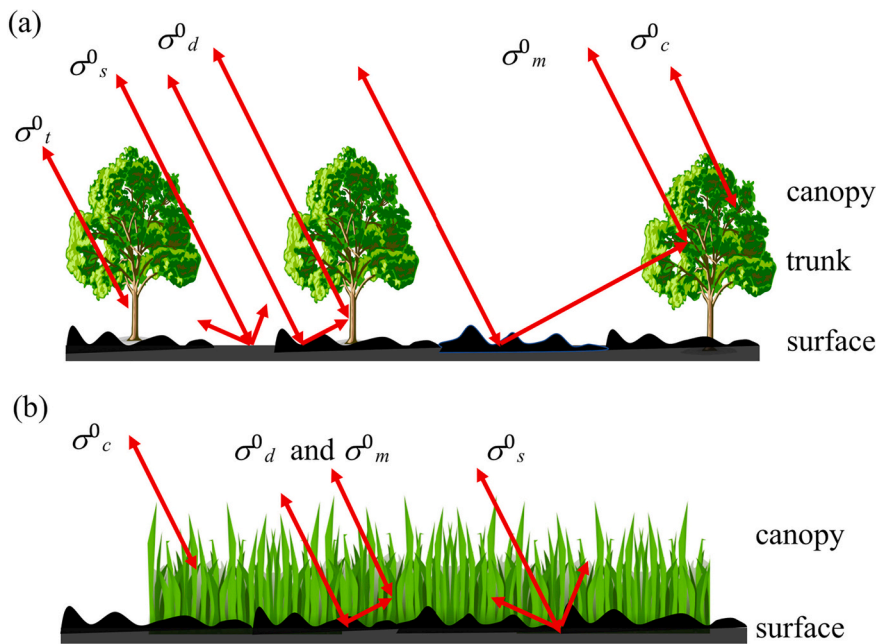
Fig. 1. Schematic plot of scattering sources from a three-layer model for woody (a) and a two-layer model for herbaceous vegetation (b). σ^0_t= direct trunk scattering; σ^0_s= ground surface scattering; σ^0_d= double-bounce scattering from ground and trunk (or stem); σ^0_m= multiple-path scattering from ground and canopy; σ^0_c= canopy scattering. This figure was modified based on Fig. 1 in Kasischke and Bourgeau-Chavez (1997) where σ^0_d was not included in the scattering model for herbaceous vegetation.

C-band Microwave Energy Scattering on Ground/Water Surfaces and Linear Relationships

Fig. 2. Schematic illustrations showing C-band microwave energy scattering from ground/water surfaces and linear relationships between co-polarized σ° (HH or VV) and d_w for three vegetation types: sparse woody, medium dense, and sparse herbaceous. The second, third, and fourth columns show scattering at different water depths. Canopy and trunk scattering are not presented for simplicity. The last column shows the detected linear relationships between C-band σ° and d_w based on previous studies and references with information on wavelengths and polarizations. Red dots denote the maximum backscatter value. Plots (a) - (c) and (e) - (g) are modified from Yuan et al. (2015) Fig. 12; (i) - (k) are modified from J.-W. Kim et al. (2014)Fig. 3(c). (For interpretation of the references to colour in this figure legend, the reader is referred to the web version of this article.)

canopy lead to stronger double-bounce scattering under the flooded state (Townsend, 2002).

Biophysical characteristics of herbaceous vegetation are also associated with double-bounce scattering. Though the original scattering model, i.e., Eqs. (2), did not include double-bounce scattering, later studies found that double-bounce scattering occurs in herbaceous wetlands depending on the height, density, and canopy covers (Pope et al., 1997; Hong et al., 2009; Hong and Wdowinski, 2011; Brisco, 2015; Wdowinski and Hong, 2015; Liao et al., 2020). A high percentage cover of tall, dense vegetation shows a backscatter increase from unflooded to flooded states due to double-bounce scattering, whereas short, sparse vegetation shows a backscatter decrease due to specular reflection of the energy (Pope et al., 1997).

2.2. Linear relationships between backscatter and water depth in wetlands

This section mainly summarizes previous studies that found linear relationships between C-band $\sigma°$ and d_w, where water depth is a proxy for the height of the vegetation above water surfaces. Significant linear relationships were only detected using co-polarized data (HH or VV) under three types of vegetation: sparse woody, medium dense, and sparse herbaceous, corresponding to positive, combined positive and negative, and negative $\sigma°$-d_w relationships, respectively.

For woody wetlands, in the unflooded state, diffuse scattering occurs from the soil surface (Fig. 2(a)). In the initial stages of flooding, the fraction of water surface is low due to ground surface micro-topography (Fig. 2(b)) (Lang and Kasischke, 2008). As water depth increases, the fraction of water surface increases, which leads to an enhancement of double-bounce scattering (Lang and Kasischke, 2008). Therefore, the correlation between $\sigma°$ (C-HH and C-VV) and d_w is expected to be positive. In contrast, Kasischke et al. (2003) found negative $\sigma°$-d_w correlations in sparsely forested wetlands using C-VV backscatter data, most likely because the reduction in surface scattering from saturated soils was greater than the increase in backscatter from ground-trunk interactions. For the L-band wavelength studies, positive $\sigma°$-d_w correlations were found using L-HH data (Yuan et al., 2015).

Backscatter from herbaceous vegetation depends on vegetation density and water depth with respect to the plant height (Pope et al., 1997; Yuan et al., 2015). When unflooded, diffuse scattering occurs from the soil surface (Fig. 2(e) and (i)). For medium dense herbaceous vegetation, significant $\sigma°$-d_w correlations have not been discovered using C-band data. However, L-HH data were correlated with water depths in shallow and deep flooded states (Yuan et al., 2015). Under shallow flooded states, backscatter increases with water depths because of enhanced double-bounce scattering (Fig. 2(f)). However, after water depth reaches a certain level with respect to the plant height, increasing water depth reduces canopy scattering, resulting in lower backscatter (Fig. 2(g)). Consequently, the $\sigma°$-d_w relationship is a combined positive and negative linear trend (Fig. 2(h), Yuan et al., 2015). Since C-band microwave energy can be transmitted through the medium dense herbaceous canopy (Hong et al., 2009; Hong and Wdowinski, 2011), though with a lower degree of transmission than L-band energy, this combined $\sigma°$-d_w relationship can also occur with C-band data.

For sparse herbaceous vegetation, increasing water depth reduces the canopy and ground-canopy scattering because more energy is forward scattered away from the SAR (Fig. 2(j) and (k)), resulting in a negative relationship between $\sigma°$ and d_w (Fig. 2(l)). Significant negative relationships were detected with C-VV data (Kasischke et al., 2003, 2009). Negative $\sigma°$-d_w correlations have also been found using L-HH data (J.-W. Kim et al., 2014; D. Kim et al., 2017a).

3. Study areas

The southern Florida Everglades wetlands are characterized by a flat topography with a minimal gradient of 2 cm per kilometer (Bourgeau-Chavez et al., 2005). The Everglades is subjected to a subtropical climate

with seasonal rainfall, in which a wet season is from May to October and a dry season from November to April. The Everglades consists of managed hydrological units (white polygons in Fig. 3(a)), including Water Conservation Areas (WCAs), Everglades National Park (ENP), and Big Cypress National Preserve (BCNP). These units are compartmentalized by canals and levees and vary in composition and relative abundance of wetland plant communities (Gunderson, 1994; Harvey et al., 2011). ENP and WCAs have a vast extent of freshwater marshes, wet prairies (herbaceous communities with a relatively short hydroperiod), and deep-water sloughs. The marshes, dominated by sawgrass (*Cladium jamaicense* Crantz), are interspersed with patches dominated by shrubs and trees (David, 1996). BCNP is characterized by a large extent of cypress forests.

Our study focused on two areas of the Everglades: the northeast Shark River Slough (NESRS) in the northeast corner of ENP and a sub-area in southern WCA-3A (S3A), varying in vegetation patterns and hydrological regimes (Fig. 3). NESRS is dominated by *Cladium* marsh, interspersed with marsh communities that are dominated by shorter graminoid species (Fig. S1). *Cladium* marsh occupies about 72% of NESRS, nearly half of which is characterized by sparse culm density (Gann et al., 2019). S3A is characterized by a ridge and slough landscape, where ridges are elevated surfaces predominantly covered with tall stands of medium to high density *Cladium* (Table 1), and open water sloughs are composed of floating and submerged vegetation with some emergent graminoid and broadleaf species (Watts et al., 2010) (Fig. 3 (c)). Both NESRS and S3A are characterized by tree islands that are patches of broadleaf forest embedded within a non-woody vegetation matrix (Heffernan et al., 2009). The tree islands occur in slightly elevated terrain and feature dense understory, including vines and ferns. Hydrological conditions in both study areas are characterized by seasonal water depth variations. Water surfaces in NESRS occasionally drop below the ground level, and the maximum water depth is about 80 cm. The majority of S3A is typically inundated throughout the year, with maximum water depth reaching 160 cm.

4. Data and data preprocessing

To understand the relationships between backscatter, water depth, and vegetation characteristics across wetland plant communities in a spatiotemporal fashion, three categories of data products were used, (1) SAR backscatter observations acquired by the Sentinel-1 platform, (2) hydrological data in form of water surface maps and corresponding DTMs, (3) two types of vegetation data products generated from optical remote-sensing observations: vegetation maps derived from WorldView-2 (WV2) data and the Normalized Difference Vegetation Index (NDVI) derived from Landsat 8 data.

4.1. SAR data and preprocessing

We obtained multi-temporal C-band data acquired by the Sentinel-1 satellite constellation (consisting of two satellites: Sentinel-1A and 1B) from the European Space Agency (ESA-https://scihub.copernicus.eu/). We only used Sentinel-1A data because they were consistently acquired almost every 12 days over the Everglades since early 2016. As our data processing began in June 2019, we used 66 Sentinel-1A scenes from the same ascending path 48, covering three full years, from April 2016 to March 2019 (acquisition dates are listed in Table S1). We used Level-1 high-resolution Ground Range Detected (GRD) products in Interferometric Wide (IW) mode, with a pixel spacing of 10 m × 10 m and a spatial resolution of 20 m × 22 m in range and azimuth directions, respectively. These products provided backscatter observations in two polarizations: C-VV and C-VH.

We processed the SAR acquisitions using the Sentinel Application Platform (SNAP) provided by the ESA. The processing included thermal noise removal, radiometric calibration, speckle filtering, and terrain correction using the 3-arcsecond Shuttle Radar Topography Mission
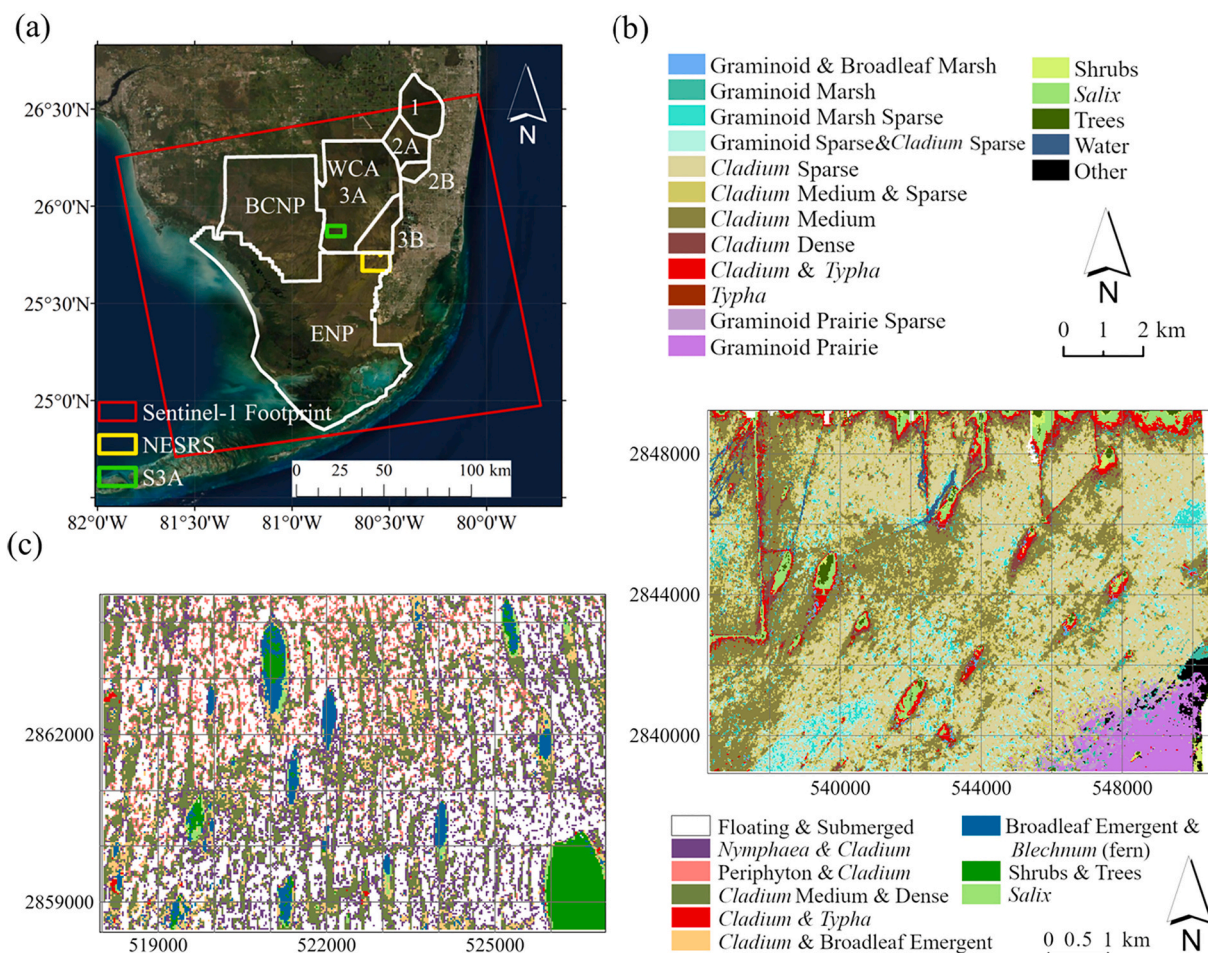
Fig. 3. (a) Location map of the main hydrological units (polygons with white boundaries) in the Florida Everglades and two study areas (yellow and green rectangles). The first study area, NESRS (yellow rectangle, 14,576 ha), is located in the northeast section of ENP. The second study area, S3A (green rectangle, 5,414 ha), is located in the southern portion of WCA-3A. The frame marked by the red line draws a footprint of the Sentinel-1A SAR scene used in this study. (b) and (c) show vegetation maps of the two study areas with a UTM coordinate system in a meter unit and a 30-m spatial resolution. Vegetation class information is provided in Table 1. The map background is a true-colour base map (Source: ESRI, DigitalGlobe, GeoEye, Earthstar Geographics, CNES/Airbus DS, USDA, USGS, AeroGRID, IGN, and the GIS User Community). (For interpretation of the references to colour in this figure legend, the reader is referred to the web version of this article.)

(SRTM). The terrain correction step used the Range Doppler method to geocode SAR scenes to the UTM coordinate system (Filipponi, 2019). Backscatter values in the processed images were sigma nought ($\sigma°$) in decibel (dB) units. We resampled the SAR images from the original pixel spacing 10 m to 30 m by bilinear interpolation to reduce speckle effects (Inglada et al., 2016), coregistered the images with the 30-m resolution Landsat grid, and stacked them by polarization.

4.2. Hydrology and DTM data

We used the interpolated Everglades Depth Estimation Network (EDEN) product of water level surface maps with 400 m × 400 m resolution (Johnston et al., 2004; Palaseanu and Pearlstine, 2008; Liu et al., 2009) to calculate water depth maps (Fig. S2). The EDEN water surface data represented daily median water levels with a vertical accuracy of about 3.3 cm (Liu et al., 2009). We obtained daily median water-level surface maps for the period of interest from April 2016 to March 2019.

We used the most accurate available ground elevation data to generate water depths for each study area. For the NESRS study area, we used the DTM derived from the Light Detection and Ranging (LiDAR) data acquired by ENP in 2017 with a spatial resolution of 0.5 m and a vertical accuracy of 34.8 cm (Dewberry, 2018). For the S3A study area, we used the 400 m resolution DTM provided by EDEN (https://sofia.usgs.gov/eden/models/groundelevmod.php). This coarser grid DTM

captured the general elevation but did not account for small-scale topographic features. Uncertainty of the estimated ground elevations in S3A was about 10 cm (Jones and Price, 2007a, 2007b). Both DTM products had the same vertical datum (North American Vertical Datum of 1988 or NAVD88) as the EDEN water surfaces. We resampled both DTM products to the 30-m Landsat grid by upscaling the high-resolution NESRS DTM using bilinear interpolation and extracting the low-resolution grid value of the S3A DTM.

4.3. Vegetation and optical remote sensing data

Vegetation classes were mapped from 2-m spatial resolution WV2 data. The 2016 and 2017 vegetation map of NESRS had an overall accuracy of 93.8 ± 1.1% (Gann et al., 2019), and the 2011 and 2012 map of S3A had an accuracy of 91.2 ± 0.6% (Gann, 2018). The 2-m resolution classes distinguished vegetation by predominant morphology, density, and species (Table 1). For example, *Cladium jamaicense*, a tall graminoid species, was recognized at the species level and was mapped at three densities: sparse, medium dense, and dense (represented by "_S", "_M", and "_D" in Table 1). Application of the multi-dimensional grid point scaling algorithm (Gann, 2019) to the 2-m resolution vegetation maps generated representative vegetation classes at the 30-m resolution of the Landsat grid (Fig. 3(b) and (c)). Upscaled vegetation classes consisted of either one original class when dominant beyond 75%, or a mix of two

Table 1

Morphological growth classes (Morphology), upscaled vegetation classes (Class Name), and species lists for each class (Class Description) for the study areas NESRS and S3A.

Morphology	Class Name	Class Description
NESRS		
Short Graminoid & Broadleaf Emergent	Graminoid (gM) & Boradleaf Marsh (blE)	Mix of patches of graminoid marsh (e.g., *Rhynchospora* spp., *Eleocharis* spp., *Panicum* spp.) and broadleaf emergent marsh (e.g., *Pontederia cordata, Sagittaria lancifolia, Crinum americanum, Thalia geniculata*)
Short Graminoid	Graminoid Marsh Medium (gM_M) Graminoid Marsh Sparse (gM_S)	Graminoid marsh (e.g., *Rhynchospora* spp., *Eleocharis* spp., *Panicum* spp.) Sparse graminoid marsh
Tall Graminoid	Graminoid Marsh Sparse (gM_S) & *Cladium* Sparse (Cl_S) *Cladium* Sparse (Cl_S) *Cladium* Medium (Cl_M) & Sparse (Cl_S) *Cladium* Medium (Cl_M) *Cladium* Dense (Cl_D) *Cladium* (Cl) & *Typha* (Ty) *Typha* Graminoid Prairie Sparse (gP_S) Graminoid Prairie Medium (gP_M)	Mix of patches of sparse graminoid marsh and sparse *Cladium jamaicense* Sparse *C. jamaicense* Mix of patches of intermediate and sparse *C. jamaicense* Intermediate density of *C. jamaicense* Dense *C. jamaicense* Mix of *C. jamaicense* and *Typha* spp. *Typha* spp. Sparse Graminoid Prairie Graminoid Prairie (e.g., *Muhlenbergia capillaris, Schizachyrium* spp., *Andropogon* spp.)
Woody	Shrubs (s) *Salix* (sSa) Trees (t)	Mix of swamp and bayhead shrub species *Salix caroliniana* Mix of swamp, hammock and bayhead tree species
NA	Water (wtr)	Open Water (e.g., canals and deep airboat trails)
S3A		
Floating Broadleaf & Submerged	Floating (blF) & Submerged (aS)	Floating *(e.g., Nymphaea odorata, Chara, Utricilaria* spp.*)* and submerged aquatic vegetation, including floating periphyton mats
Floating/Submerged & Tall Graminoid	*Nymphaea* (blFNy) & *Cladium* (Cl) Periphyton (aSPe) & *Cladium* (Cl)	Mix of patches of *N. odorata* and *C. jamaicense* Mix of patches of Periphyton and *C. jamaicense*
Tall Graminoid	*Cladium* Medium & Dense (Cl_M & Cl_D) *Cladium* (Cl) & *Typha* (Ty)	Intermediate to dense *C. jamaicense* Mix of *C. jamaicense* and *Typha* spp.
Tall Graminoid & Broadleaf Emergent	*Cladium* (Cl) & Broadleaf Emergent (blE)	Mix of patches of *C. jamaicense* and broadleaf emergent marsh (e.g., *Peltandra virginica, P. cordata, S. lancifolia, C. americanum*)
Broadleaf Emergent	Broadleaf Emergent (blE) & *Blechnum* (fern) Marsh (blEBl)	*Blechnum serrulatum* (fern) and other broadleaf emergent marsh (e.g., *P. virginica, P. cordata, S. lancifolia, C. americanum*)
Woody	Shrubs & Trees (s & t) *Salix* (sSa)	Mix of hammock and bayhead shrub and tree species *S. caroliniana*

classes for more diverse grid cells (e.g., "Medium & Sparse *Cladium*" in NESRS, Table 1), with the additional requirement that each scaled class covered at least 5% of the study area. The vegetation map was considered valid during our period of interest from April 2016 to March 2019 because most vegetation (e.g., the dominant *Cladium*) showed minimal seasonal or annual structural variations (Steward and Ornes, 1975). Only small areas in NESRS were impacted by fires in 2017 and 2018 (Malone, 2019) (Fig. S3), the main driver for rapid change in vegetation cover. For the fire-impacted areas, the vegetation maps represent the vegetation classes before the fire events.

We obtained *Cladium* height and biomass data in NESRS and S3A from field surveys conducted from 2016 to 2019 (Ross et al., 2016; Kalla and Scheidt, 2017; Sah et al., 2020). The height data were from sampling plots within the two study areas, whereas the biomass data were from *Cladium* samplings across the entire ENP and WCA-3A to represent the NESRS and S3A biomass, respectively. Details of the vegetation characteristics data are provided in Supplementary Note 1 and Fig. S4. These data were used to compare with vegetation characteristics in previous studies on wetland backscatter behavior.

NDVI derived from optical remote-sensing data is sensitive to vegetation density, which can potentially affect microwave scattering behavior (Gitelson, 2004; Gasparri et al., 2010; Zhang et al., 2016). NDVI combines the red (RED) and near-infrared (NIR) bands using the equation $NDVI = (NIR - RED)/(NIR + RED)$ and ranges from −1.0 to 1.0. Since NDVI values can be affected by surface water depths (Han and Rundquist, 2003; Beget and Di Bella, 2007), we selected a Landsat NDVI
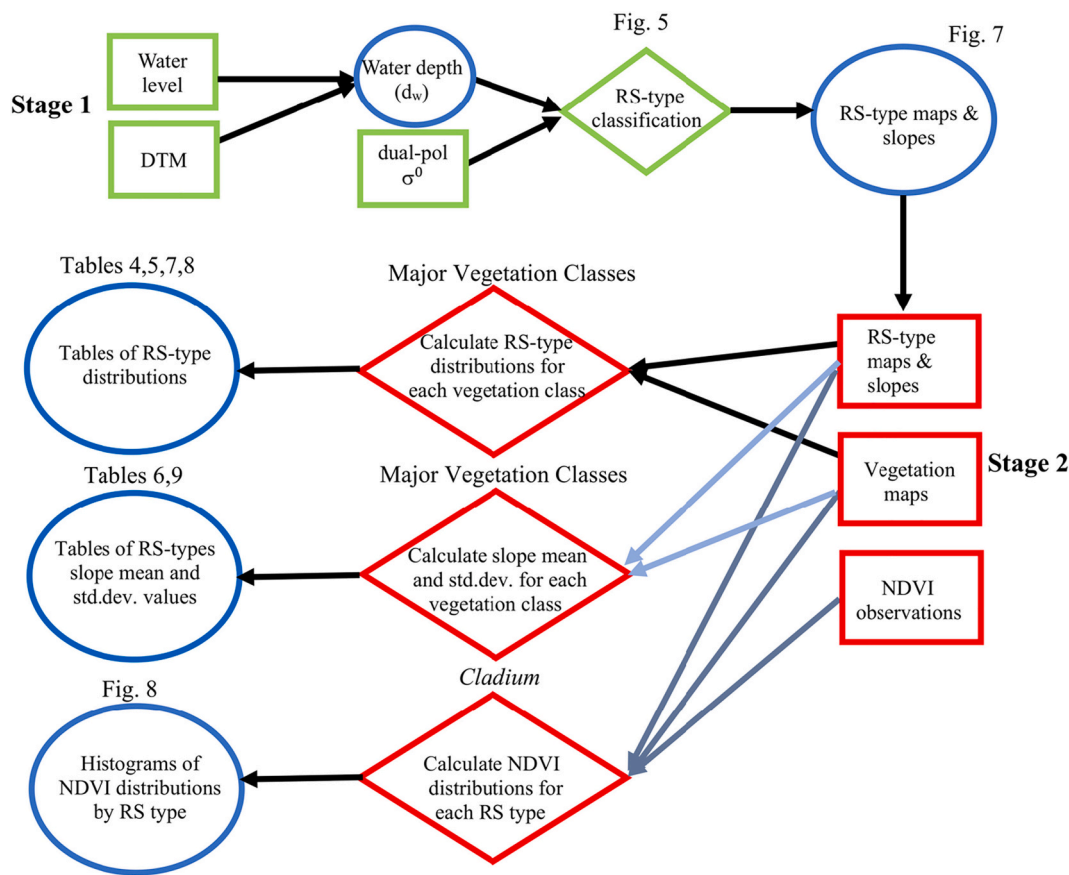
Fig. 4. Flow chart of the two-stage methodology for investigating the roles of water depth (Stage 1) and vegetation characteristics (Stage 2) on dual-polarized backscatter. Green boundaries denote Stage 1, and red boundaries denote Stage 2 procedures. Rectangles represent data, diamonds represent analyses, and blue ellipses represent results. The results of the first stage, RS-type classification maps and slopes of σ°-d$_w$ linear relationships, are the input for the second stage. (For interpretation of the references to colour in this figure legend, the reader is referred to the web version of this article.)

image acquired on April 19, 2018, within the observation period of our study when water depths were the lowest. The Landsat 8 Operational Land Imager (OLI) satellite NDVI image obtained from the U.S. Geological Survey Earth Resources Observation and Science Center (Vermote et al., 2016) had minimal cloud or cloud shadow pixels in either study area.

5. Methodology

Our main analysis of the Sentinel-1 data was a two-stage procedure (Fig. 4). In the first stage (discussed in Section 5.1), we evaluated the direction (positive or negative) and the strength (measured by R^2 and p-value) of linear relationships between σ° and d$_w$ values over the three-year period for each 30 m × 30 m pixel. Pixels showing a strong linear correlation (R^2 larger than a threshold, R^2_{th}, and p-value less than a threshold, p_{th}) were termed reliable scatterers (RS). Based on the described σ°-d$_w$ relationships according to vegetation types in Section 2.2, we defined three RS types: positive (RS$^+$), positive-negative (RS$^\pm$), and negative (RS$^-$). A fourth, non-RS type, indicated that the linear relationships between σ° and d$_w$ were weak ($R^2 < R^2_{th}$ or $p > p_{th}$). The method for classifying RS and non-RS types was provided in Section 5.1. In the second stage (discussed in Section 5.2), we investigated RS types in relation to vegetation types.

5.1. Reliable Scatterer (RS) classification

The first stage of the methodology classified pixels as one of four pixel types (RS$^+$, RS$^\pm$, RS$^-$, and non-RS) using multi-temporal σ° and d$_w$ values. The analyses of multi-temporal σ° observations separately used

C-VV and C-VH data for RS-type classification. We subtracted 30-m re-scaled DTM values from the 400-m resolution EDEN daily median water level surfaces to get 30-m resolution multi-temporal water depth maps (Fig. 4, Fig. S2). We removed all negative water depth values (groundwater) and their corresponding σ° observations (Fig. 5) because our study mainly investigated the impact of surface water on back-scatter. We excluded an outlier SAR scene acquired on September 10, 2017, during the passage of Hurricane Irma over South Florida because the C-VH backscatter values significantly deviated from the σ°-d$_w$ linear models, possibly due to additional microwave energy scattered from water surface waves induced by wind. For the areas within NESRS impacted by fires, a revised RS classification method is provided in Supplementary Materials Note 2.

Then, we classified each pixel as an RS type following the decision tree described in Fig. 5, which consisted of two steps. The first step pre-classified a pixel into one of the three RS candidates using σ° and d$_w$ values without considering the strength of correlation (R^2). We first identified d$_w$ corresponding to the maximum observed σ° (d$_w$(σ°$_{max}$), represented by the red dots in Fig. 2) for each pixel. Second, we counted the numbers of d$_w$ values higher and lower than d$_w$(σ°$_{max}$), which were termed n$_{high}$ and n$_{low}$, respectively. The number of values above (n$_{high}$) and below (n$_{low}$) reflected the relative position of d$_w$(σ°$_{max}$) in the σ°-d$_w$ diagrams (Fig. 2(d), (h), and (l)), and indicated possible RS types. For example, when n$_{high}$ equaled zero, d$_w$(σ°$_{max}$) was the highest d$_w$ value in the time series, indicating the pixel can potentially be an RS$^+$ (Fig. 2(d)). We applied a tolerance threshold (n$_{th}$), representing the minimum number of data points indicative of a significant linear trend. We initially set n$_{th}$ as 7, representing ~10% of the total 66 SAR acquisitions used in this study. The n$_{th}$ was used to compare with n$_{high}$ and n$_{low}$ to
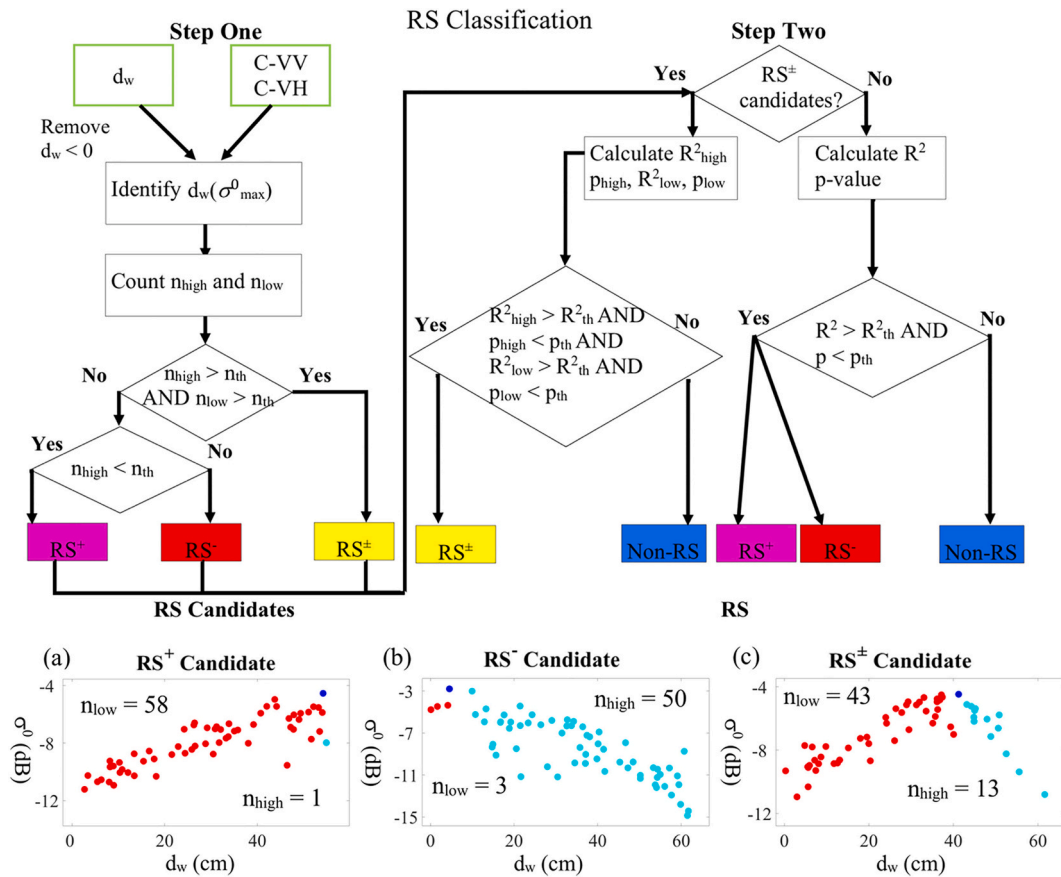
Fig. 5. Decision tree for RS classification. The tree is composed of data (rectangles with green boundary), operations (rectangles with white background and black boundary), conditions (diamonds), and endpoints (rectangles with colored background). Different background colors, i.e., pink, yellow, red, and blue, denote RS^+, $RS^\pm$, RS^- (or the corresponding candidates), and non-RS, respectively. (a), (b), and (c) σ°-d_w scatter plots examples for RS^+, $RS^\pm$, and RS^- candidates, respectively, with the x-axis representing d_w and the y-axis representing σ°. A blue dot marks the σ°_{max} point for each scatter plot; red and cyan dots represent observations with d_w less and greater than $d_w(\sigma^\circ_{max})$ and their count numbers, n_{high} and n_{low}, are to compare to n_{th} (7) to determine the RS candidate type. (a) shows n_{high} (1) is lower than n_{th} and, therefore, the pixel is classified as an RS^+ candidate, indicating the majority of the observations follow a positive trend. (b) is classified as an RS^- candidate because n_{low} (3) is smaller than n_{th}, indicating that all observations follow a negative trend. (c) displays that both n_{high} and n_{low} are higher than n_{th} and, therefore, the pixel is classified as an $RS^\pm$ candidate. (For interpretation of the references to colour in this figure legend, the reader is referred to the web version of this article.)

pre-classify each pixel into an RS^+, $RS^\pm$, or RS^- candidate (the left column in Fig. 5). When $n_{high} < n_{th}$, a pixel was pre-classified as an RS^+ candidate; when $n_{low} < n_{th}$, a pixel was pre-classified as an RS^- candidate; when both n_{high} and n_{low} were larger than n_{th}, a pixel was pre-classified as an $RS^\pm$ candidate (R^2 values to be examined in the next step for the RS^+, $RS^\pm$, or RS^- candidates). To illustrate this method of classifying RS^+, $RS^\pm$, and RS^- candidates, σ°-d_w correlation plots of three pixel examples are presented in Fig. 5(a), (b), and (c).

The second step evaluated the strength of the correlation for RS candidates using an R^2 and p-value threshold to classify each pixel as either one of the four RS types (the right column in Fig. 5). An RS candidate with an R^2 greater than the threshold R^2_{th} and a p-value less than the threshold p_{th} (as mentioned in the RS definition) was classified as the corresponding RS type; when the R^2 was smaller or the p-value was larger, an RS candidate was classified as a non-RS. Note that for an $RS^\pm$ candidate, two sets of values, R^2_{high}, p_{high}, and R^2_{low}, p_{low} were calculated for d_w values higher and lower than $d_w(\sigma^\circ_{max})$, respectively (Fig. 5(c)). It required that both sets of parameter criteria (R^2_{high}, p_{high}, and R^2_{low}, p_{low}) were satisfied to be an $RS^\pm$. We set an initial value of R^2_{th} as 0.5 (equivalent to a correlation coefficient of 0.71) and p_{th} as 0.04, based on the σ°-d_w correlation values determined by a previous study (Kasischke et al., 2009).

The second step also calculated slope values of σ°-d_w correlations for RS^+, $RS^\pm$, and RS^- candidates using the linear least-squares method. For an RS^+ or RS^- candidate, only one slope value was estimated, whereas,

for an $RS^\pm$ candidate, two slope values were estimated for the positive and negative trends, respectively.

We applied the two-step RS-type classification to each 30 m × 30 m pixel for C-VV and C-VH data separately, resulting in two RS-type classification maps for each study area. The RS-type classification relied on two critical thresholds: n_{th} and R^2_{th}. We conducted a sensitivity analysis for these two parameters by evaluating RS-type classifications with different n_{th} and R^2_{th} values (n_{th} of 2, 4, 10, and 20; R^2_{th} of 0.3 and 0.7) other than the initial values (n_{th} of 7 and R^2_{th} of 0.5). The sensitivity test used a constant p_{th} value of 0.04. Another sensitivity test was conducted to investigate the minimum number of SAR images needed to accurately classify the RS type. We used one-year and two-year SAR data to classify RS types and compared the results to the three-year ones. The results of the sensitivity analysis are presented in Supplementary Materials Note 3, Table S2, and Table S3.

We also conducted a similar σ°-d_w correlation analysis using data acquired during unflooded periods ($d_w < 0$), which only occurred in the NESRS study area. According to J.-W. Kim et al. (2017b), positive correlations between σ° and groundwater levels are expected. Therefore, we selected pixel locations with a significant number of SAR images (no less than n_{th}) acquired during unflooded periods to detect positive σ°-d_w correlations ($R^2 > R^2_{th}$ and $p < p_{th}$).
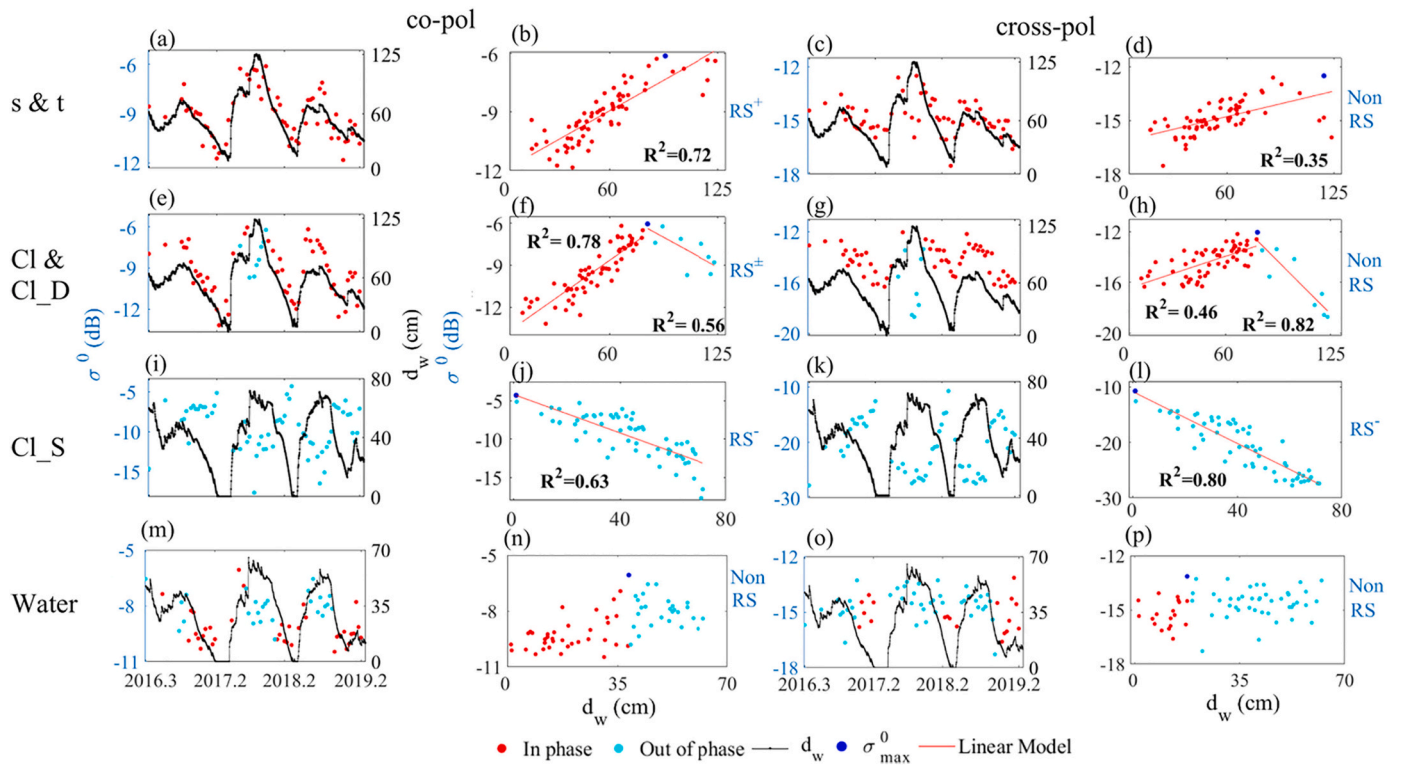
Fig. 6. Four representative pixels (in row-major order) with distinct scattering behavior are presented according to C-VV (the first two columns) and C-VH (the last two columns) $\sigma°$. Row one represents a pixel from the "Shrubs & Trees" (s & t) class in S3A; row two "*Cladium* Medium & Dense" (Cl & Cl_D) in S3A; row three "*Cladium* Sparse" (Cl_S) in NESRS; row four "Water" in NESRS. Column one (a, e, i, and m) displays time series of C-VV $\sigma°$ (including red and cyan dots with values presented on the left y-axes) and daily median d_w (black dash-dot line with values shown on the right y-axes) measured from April 2016 to March 2019 (time presented in decimal year format on the x-axes). Red dots indicate $\sigma°$ in phase with d_w; cyan dots indicate $\sigma°$ out of phase with d_w. All negative d_w values are replaced with zero. Column two (b, f, j, n) shows scatter plots of $\sigma°$ versus d_w. Red and cyan dots are the same as (a, e, i, m); blue dots mark the $\sigma°_{max}$ observations. The lines are the least-squares best-fit linear models. Column three (c, g, k, o) and four (d, h, l, p) show the time series of C-VH $\sigma°$ and d_w, and scatter plots of C-VH $\sigma°$ and d_w, respectively. (For interpretation of the references to colour in this figure legend, the reader is referred to the web version of this article.)

Table 2
Summary of the slope, R^2 and *p*-values for regression lines for four examples. 'Medium & Dense *Cladium*' class has two values for slope, R^2, and p-value, corresponding to the positive and negative trends of the combined $\sigma°$-d_w linear relationship.

Pixel Examples	C-VV						C-VH					
	Slope (dB/cm)		R^2		p-value		Slope (dB/cm)		R^2		p-value	
Shrub & Tree		0.05		0.72		<0.01		0.02		0.35		<0.01
Medium & Dense *Cladium*	0.08	−0.07	0.78	0.56	<0.01	0.02	0.04	−0.13	0.46	0.82	<0.01	0.02
Sparse *Cladium*		−0.13		0.63		<0.01		−0.23		0.80		<0.01
Water	0.04	0	0.2	0.0	0.0	0.76	0.0	0.0	0.0	0.0	0.9	0.7

5.2. Analysis of RS types in relation to vegetation characteristics

The second stage of the methodology analyzed vegetation density and morphology effects on the relationships between $\sigma°$ and d_w, using the RS-type classification maps, vegetation maps, and NDVI observations, all of which were co-registered at the Landsat 30-m grid. First, we calculated RS-type distributions (relative occurrences in percentages of four RS-types) by vegetation class and compared the RS-type distributions (1) between vegetation classes of the same morphology but different densities, and (2) between vegetation classes of different morphologies but similar densities.

Since the vegetation classes only provided classification labels on vegetation density (e.g., sparse, medium dense), we also evaluated class-specific NDVI observations to investigate the effect of relative density on RS types. NDVI cannot be used to compare vegetation densities between different vegetation types because NDVI is also associated with other biophysical vegetation parameters, such as canopy structure and chemical content (Gamon et al., 1995). Therefore, NDVI was used conditionally for vegetation densities of *Cladium* vegetation only, which had dominant spatial coverages in both study areas and was characterized by a significant range of densities (Fig. 3(b) and (c)), allowing us to understand the density effects on scattering behavior.

We used the Wilcoxon rank-sum statistical test to evaluate if the median NDVI values were significantly different between RS types (Fig. 8). The analysis was done for *Cladium* pixels in NESRS that included the four density classes: "Sparse", "Medium & Sparse", "Medium", and "Dense", and for the "Medium & Dense *Cladium*" class in S3A.

6. Results

6.1. Examples of four representative pixels

6.1.1. RS types of four pixels

Four pixels representing different vegetation/water covers illustrated the scattering behavior of RS$^+$, RS$^±$, RS$^-$, and non-RS versus water depth variations, respectively (Fig. 6).

For the "Shrubs & Trees" class example, variations in both C-VV and C-VH σ° followed similar trends as water depth changes in the time domain (Fig. 6(a) and (c)), resulting in positive linear relationships between σ° and d_w (Fig. 6(b) and (d)). However, the correlation in C-VV σ° was stronger than C-VH. Consequently, this pixel was classified as an RS$^+$ for C-VV σ°, but as non-RS for C-VH according to the R^2 values (Table 2).

For the "Medium & Dense *Cladium*" class example, the majority of the C-VV σ° were in the same phase with d_w variations, with some exceptions (i.e., in the middle part of the time series when water depth values were high, and σ° and d_w were out of phase (Fig. 6(e)). The correlation plot of C-VV σ° observations indicated a combined positive and negative relationship with d_w, both with high R^{2}s (Fig. 6(f)). However, the negative trend showed a weaker statistical significance (p-value = 0.02) compared to the positive trend (p-value <0.01) because of a fewer number of acquisitions. C-VH σ° displayed a similar combination pattern of positive and negative linear relationships (Fig. 6(h)) with a weaker positive relationship but a stronger negative relationship with d_w than C-VV. Consequently, this pixel was classified as an RS$^±$ for C-VV σ° but a non-RS for C-VH (an RS$^±$ required both positive and negative linear trends' R^{2}s higher than R$^2_{th}$).

For the "Sparse *Cladium*" class pixel, the time series of both C-VV and C-VH σ° observations were out of phase with d_w (Fig. 6(i) and (k)). Though strong negative σ°-d_w relationships occurred for both C-VV and C-VH σ°, C-VV σ° had a weaker correlation (Fig. 6(j)) than C-VH (Fig. 6(l)). Consequently, this pixel was classified as RS$^-$ for both polarizations.

For the "Water" class pixel, as expected, there was no linear correlation between σ° and d_w in areas covered by water but having no vegetation (Fig. 6(n) and (p)), and the pixel was classified as a non-RS for both polarizations because of low R^2 values and high p-values (Table 2).

6.1.2. Slopes of regression lines for the four pixels

For the "Shrubs & Trees" example, the σ°-d_w regression lines showed positive slope values of 0.05 and 0.02 db/cm for C-VV and C-VH σ°, respectively (Table 2). For the "Medium & Dense *Cladium*" example with a combined σ°-d_w relationship, the positive and negative slope values were 0.08 and −0.07 dB/cm for C-VV σ°, and 0.04 and −0.13 dB/cm for C-VH σ°. For the "Sparse *Cladium*" example, the negative slope values were −0.13 and −0.23 dB/cm for C-VV and C-VH σ°, respectively. The "Water" pixel showed two slope values for each polarization because it was classified as a RS$^±$ candidate in the first RS classification step, and all slope values were close to zero.

6.2. RS-type classification for the NESRS and S3A study areas

Fig. 7 presents the classification results based on RS type. NESRS was dominated by RS$^-$ and non-RS types, with negligible RS$^+$ and RS$^±$ type pixels. For C-VV σ°, the non-RS type was dominant (76%), and the RS$^-$ type (20%) was mainly located in areas with the "Sparse *Cladium*" class (Fig. 3(b)). However, for C-VH σ°, RS$^-$ type was dominant (68%), and non-RS type (32%) was mostly located in areas with woody vegetation, including the northern and western edges and tree islands in the middle of the study area (Fig. 7(b), Fig. 3(b)). More than 99% of RS$^-$ type pixels had p-values less than 0.001 for both C-VV and C-VH σ°.

In S3A, RS$^+$ and RS$^±$ types were frequent for C-VV and RS$^-$ type for C-VH σ°, though the non-RS type was dominant for both polarizations. For C-VV, RS$^+$ type (5%) was located on tree islands, corresponding to the "Shrubs & Trees" class (Fig. 3(c)), and RS$^±$ type (15%) was located on ridges, corresponding to the "Medium & Dense *Cladium*" class. For C-VH σ°, the RS$^+$ type pixels (2%) were also located on tree islands but with a lower number than those for C-VV. RS$^-$ type pixels (23%) were located in slough vegetation. More than 99% of RS pixels (including
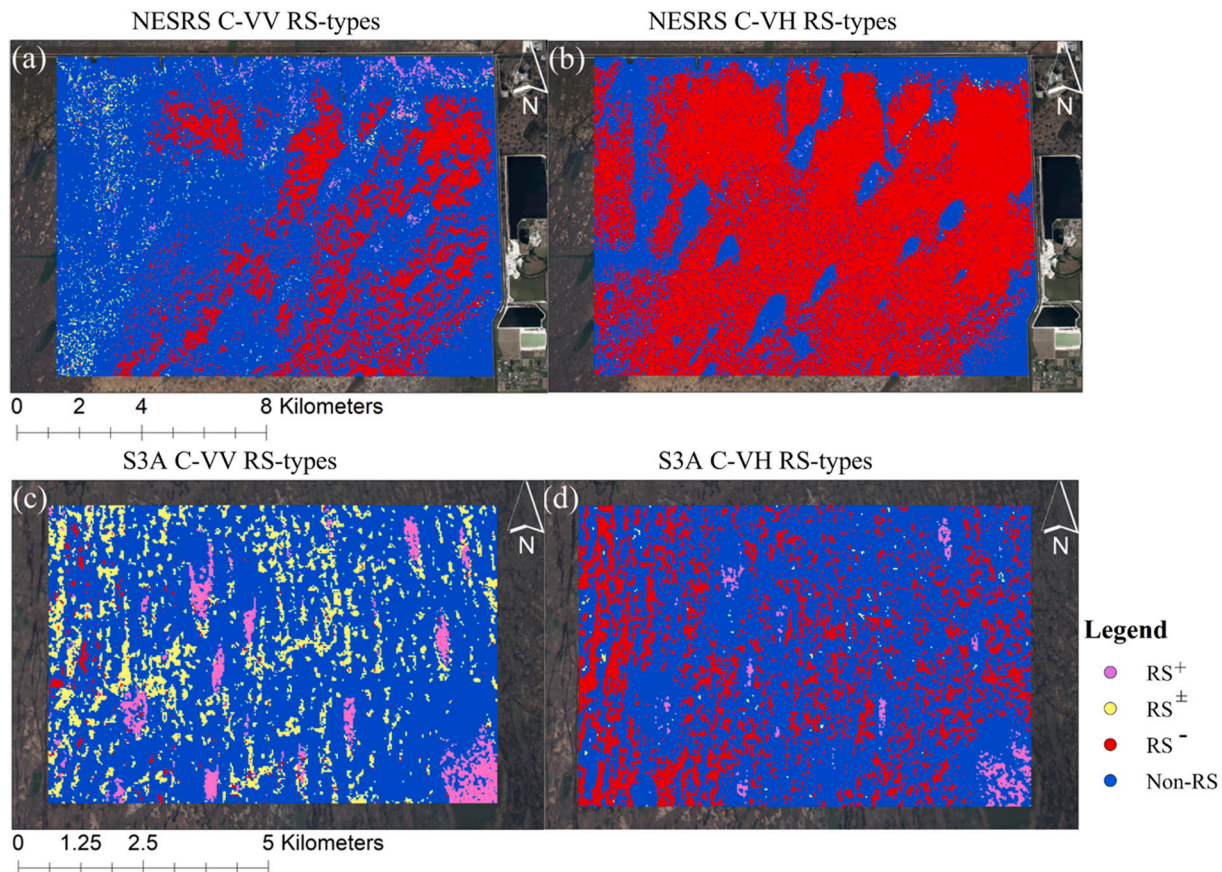

Fig. 7. Spatial distribution of RS types in NESRS (a, b) and S3A (c, d). (a) and (c) show RS types for C-VV σ°. (b) and (d) show RS types for C-VH σ°.

Table 3

Relative coverages (%) of main vegetation types in NESRS and S3A.

NESRS Vegetation	Percentage	S3A Vegetation	Percentage
Cladium Sparse	27	Floating & Submerged	39
Cladium Medium	24	*Cladium* Medium & Dense	23
Cladium Medium & Sparse	19	*Nymphaea* & *Cladium*	15
Graminoid Marsh Sparse & *Cladium* Sparse	7	Periphyton & *Cladium*	7
Graminoid Prairie Medium	3	*Cladium* & Broadleaf Emergent	5
Cladium & *Typha*	3	Broadleaf & *Blechnum*	3
Cladium Dense	2	Shrubs & Trees	3
Graminoid Marsh Sparse	2	*Salix*	1
Graminoid Marsh Medium	2		
Salix	2		
Tree	1		
Graminoid Prairie Sparse	1		

RS$^+$, RS$^\pm$, RS$^-$) had *p*-values less than 0.001 for both C-VV and C-VH σ°, except that 50% and 81% of RS$^\pm$ type pixels had p-values of the negative linear trends (p$_{low}$) less than 0.001 for C-VV and C-VH σ°, respectively.

Our RS-type classification method successfully classified the majority of pixels in both study areas, but noisy σ° observations or DTM errors at times caused misclassification of RS$^+$ or RS$^-$ types as non-RS. For a more detailed discussion and solution, see Supplementary Materials Note 4 and Fig. S5.

The sensitivity test of R^2 showed that as R$^2_{th}$ increased from 0.3 to 0.7, the percentage of RS types (including RS$^+$, RS$^\pm$, and RS$^-$) decreased significantly (Table S2). However, variations in n$_{th}$ from 2 to 20 had a limited impact on the percentage of RS (< 8%). Sensitivity tests for different lengths of SAR time series (one and two years) indicated that the difference of RS-type distribution between one-year and three-year time series was more significant than the difference between two-year and three-year time series (Table S3). In S3A, the percentages of different RS-types between time series were larger than those for NESRS.

6.3. Analysis of RS types in relation to vegetation characteristics

This section presents RS-type distributions for the major vegetation classes by study area (Section 6.3.1), and NDVI distributions by RS type for *Cladium* dominated vegetation classes in both study areas (Section 6.3.2).

6.3.1. RS-type distributions based on vegetation classes

6.3.1.1. NESRS study area. Table 3 presents relative spatial coverages of 12 major vegetation classes in NESRS, representing three morphological categories: tall graminoid, short graminoid, and woody

vegetation according to Table 1. RS-type distributions varied with density class within the same growth morphology. For *Cladium*, a tall graminoid species with four density classes, RS-type distributions for C-VV σ° showed that only "Sparse *Cladium*" had a considerable RS$^-$ type percentage (Table 4), and the other three *Cladium* classes with higher densities were dominated by the non-RS type. For C-VH σ°, RS$^-$ type percentage decreased, and non-RS type percentage increased as vegetation density increased. The other two vegetation types, "Graminoid Prairie" and "Graminoid Marsh", showed similar behavior in their sparse density classes displaying higher RS$^-$ type percentages than the corresponding medium density classes for both polarizations (Table S4).

RS-type distributions were different between tall and short growth morphologies with similar densities (Table 5), with *Cladium* and "Graminoid Prairie" representing tall growth morphology, and "Graminoid Marsh" the short growth morphology. To avoid the density effect on RS-type distributions, we only compared sparse density classes. Both tall and short morphology groups included only two RS types: RS$^-$ and non-RS, but tall graminoids had higher RS$^-$ type percentages than short graminoids for both polarizations. The slope values of these major herbaceous vegetation were summarized in Table 6. Finally, the woody classes, "*Salix*" and "Tree", were dominated by the non-RS type in both polarizations (Table 7).

The slope values were generated from linear regression analysis for seven major vegetation types characterized by significant RS$^-$ type percentages (Table 6 and S4). For each vegetation type, slopes for C-VV σ° were always shallower than those for C-VH. *Cladium* and "Graminoid Marsh" vegetation types had shallower slopes compared to "Graminoid Prairie".

We also detected a significant number of RS$^+$ type pixels using σ° and d$_w$ data during unflooded periods (d$_w$ < 0) in NESRS (Table S5). To

Table 4

RS-type distributions for *Cladium* vegetation classes in both NESRS and S3A.

Study area	Morphology	Vegetation Class	RS-type percentages (%) C-VV				RS-type percentages (%) C-VH			
			RS$^+$	RS$^\pm$	RS$^-$	Non-RS	RS$^+$	RS$^\pm$	RS$^-$	Non-RS
NESRS	Tall Graminoid	*Cladium* Sparse	0	0	46	54	0	0	95	5
		Cladium Medium & Sparse	0	1	11	88	0	0	83	17
		Cladium Medium	2	5	3	90	0	0	56	44
		Cladium Dense	8	2	2	88	1	0	3	96
S3A		*Cladium* Medium & Dense	1	46	2	51	0	1	7	92

Table 5

RS-type distributions for "Tall" and "Short Graminoid" morphologies in NESRS.

Morphology	Vegetation Class	RS type percentages (%) C-VV				RS type percentages (%) C-VH			
		RS$^+$	RS$^\pm$	RS$^-$	Non-RS	RS$^+$	RS$^\pm$	RS$^-$	Non-RS
Tall Graminoid	*Cladium* Sparse	0	0	46	54	0	0	95	5
	Graminoid Prairie Sparse	0	0	64	36	0	0	86	14
Short Graminoid	Graminoid Marsh Sparse	0	1	28	71	0	0	78	22

Table 6

Slope mean and standard deviation (dB/cm) values for major vegetation types in NESRS calculated using all RS⁻ type pixels for each vegetation type. (Values are omitted if the RS⁻ type percentage is smaller than 15%.)

	VV			VH		
Vegetation Class	Mean	Std. Dev.	Number of RS⁻ Pixels	Mean	Std. Dev.	Number of RS⁻ Pixels
Cladium Sparse	-0.13	0.03	20,037	-0.23	0.04	41,706
Cladium Medium	*	*	*	-0.17	0.05	21,560
Cladium Medium & Sparse	*	*	*	-0.20	0.05	25,912
Graminoid Prairie Sparse	-0.18	0.05	1,068	-0.30	0.09	1,430
Graminoid Prairie Medium	-0.22	0.08	1,349	-0.39	0.15	2,143
Graminoid Marshes Sparse	-0.13	0.03	1,038	-0.18	0.04	2,940
Graminoid Marshes Medium	*	*	*	-0.16	0.06	1,817

distinguish these pixels from the RS⁺ type detected during the flooded state, we termed them unflooded RS⁺. More unflooded RS⁺ type pixels were detected using C-VV σ° (38,128; 24% of the total number of pixels) than C-VH (3,693; 2%). Unflooded RS⁺ type was detected in all major vegetation types in NESRS, and the majority of unflooded RS⁺ type pixels were found in *Cladium*, the dominant vegetation type. *Cladium* and Graminoid Prairie (each including multiple density levels) were characterized by large percentages of the unflooded RS⁺ type for C-VV data. Shrub and tree vegetation types also had unflooded RS⁺ type pixels, but with a lower percentage (Table S5).

6.3.1.2. S3A study area. The RS-type distribution of three major vegetation classes in S3A: "Floating & Submerged", "*Nymphaea & Cladium*", and "Periphyton & *Cladium*" were very similar (Table 8). Non-RS was the most dominant pixel type for C-VV σ°, whereas both RS⁻ and non-RS types were the most abundant for C-VH σ°. C-VV σ° results showed the "*Nymphaea & Cladium*", and "Periphyton & *Cladium*" classes had larger

RS± type percentages than the "Floating & Submerged" class. Another major class, "Medium & Dense *Cladium*" had considerable RS± type percentages for C-VV σ° and dominant non-RS type for C-VH σ° (Table 4).

Woody classes ("Shrubs & Trees" and "*Salix*") had considerably higher RS⁺ type percentages for C-VV than C-VH σ° (Table 7). The "Broadleaf Emergent & *Blechnum* (fern) Marsh" class resembled RS-type distributions of woody vegetation for many RS⁺ type pixels in both polarizations (Table 7).

Overall, RS-type distributions significantly varied with the three major morphologies (Table S6). "Floating/Submerged & Tall Graminoid" morphology had many RS⁻ type pixels in C-VH, "Tall Graminoid" morphology class "Medium & Dense *Cladium*" had many RS± type in C-VV, and "Woody" and "Broadleaf Emergent" morphologies for RS⁺ type in both polarizations.

For the RS⁺ type, linear model slopes (Table 9) showed similar mean values (about 0.04 dB/cm) for vegetation types "*Salix*", "Shrubs and

Table 7

RS-type distributions of "Woody" and "Broadleaf Emergent" morphology.

Study area	Morphology	Vegetation Class	RS type percentages (%) C-VV				RS type percentages (%) C-VH			
			RS⁺	RS±	RS⁻	Non-RS	RS⁺	RS±	RS⁻	Non-RS
NESRS	Woody	*Salix*	4	1	0	95	1	0	0	99
		Tree	0	0	3	97	0	0	4	96
S3A	Woody	Shrubs & Trees	47	0	0	53	26	0	0	74
		Salix	43	4	2	51	5	0	0	95
	Broadleaf Emergent	Broadleaf Emergent & *Blechnum* (Fern) Marsh	58	0	0	42	21	0	0	79

Table 8

RS-type distributions of "Floating/Submerged & Tall Graminoid" morphology in S3A.

Morphology	Vegetation Class	RS type percentages (%) C-VV				RS type percentages (%) C-VH			
		RS⁺	RS±	RS⁻	Non-RS	RS⁺	RS±	RS⁻	Non-RS
Floating Broadleaf & Submerged	Floating & Submerged	0	0	0	100	0	0	29	71
Floating/ Submerged & Tall Graminoid	*Nymphaea & Cladium*	1	10	0	89	0	0	28	72
	Periphyton & *Cladium*	0	8	0	92	0	0	30	70

Table 9

Slope mean and standard deviation values (dB/cm) for major vegetation types in S3A for RS⁺, RS±, and RS⁻ types. Standard deviation values are presented in brackets. (Values are omitted if a RS type percentage is smaller than 15% or not applicable.)

|		VV			VH		
RS type	Vegetation Class	Positive Slope	Negative Slope	Number of RS	Positive Slope	Negative Slope	Number of RS
RS⁺	*Salix*	0.04 (0.01)		280			
	Shrubs & Trees	0.04 (0.01)		1,049	0.04 (0.00)		575
	Broadleaf & *Blechnum*	0.04 (0.01)		868	0.04 (0.00)		315
RS±	*Cladium* Medium & Dense	0.07 (0.01)	-0.1 (0.03)	6,443			
	Cladium & Broadleaf	0.07 (0.01)	-0.1 (0.03)	1,007			
RS⁻	Floating & Submerged					-0.07 (0.01)	3,422
	Nymphaea & Cladium					-0.07 (0.01)	2,610
	Periphyton & *Cladium*					-0.07 (0.01)	1,348
	Cladium & Broadleaf					-0.08 (0.02)	660
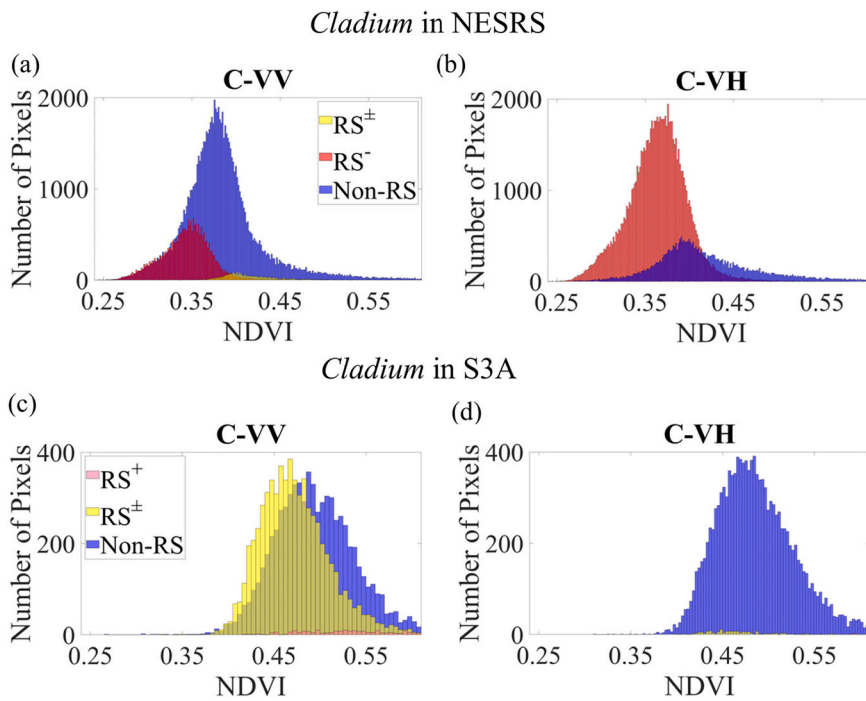
Cladium in NESRS

Fig. 8. Histograms of NDVI values for (a, b) *Cladium* in NESRS comprising all four density classes; (c, d) the "Medium and Dense *Cladium*" class in S3A. RS types were classified using C-VV σ° (a, c) or C-VH σ° (b, d). Four sub-images share the same NDVI ranges for comparison, which shows NDVI values of NESRS *Cladium* are less than S3A *Cladium*. NESRS *Cladium* RS⁻ type in C-VV σ° (a) has an NDVI value range from 0.25 to 0.35, narrower than that in C-VH (0.25–0.45). Transparency is set for the front layers of each sub-images to reveal the non-RS type background layer.

Trees", and "Broadleaf & *Blechnum*" for both C-VV and C-VH σ°. For the RS± type, "*Cladium* Medium and Dense" and "*Cladium* and Broadleaf' showed similar positive (0.07 dB/cm) and negative (−0.1 dB/cm) slope means in C-VV σ°. For the RS⁻ type, four vegetation types shared similar slope means (about −0.07 dB/cm) for C-VH σ°, including "Floating and Submerged", "*Nymphaea & Cladium*", "Periphyton and *Cladium*", and "Broadleaf and *Cladium*". Slope standard deviations were no more than 0.03 dB/cm for each vegetation type.

C-band Microwave Energy Scattering on Ground/Water Surfaces and Linear Relationships

Fig. 9. Schematic illustrations of the suggested C-band microwave energy scattering from the ground or water surfaces and linear σ°-d_w relationships for both C-VV and C-VH σ° for the same vegetation types with Figure 2. The text in each grid presents the dominant scattering mechanism(s). Dashed lines in (e) and (j) denote weaker linear relationships (less R²) and less sensitivity (shallower slope) to variations in water depths in C-VH observations than C-VV, and the bold lines in (j) and (o) denote stronger linear relationships and greater sensitivity to variations in water depths than C-VV.

6.3.2. NDVI analysis by RS type for Cladium

In NESRS, for the *Cladium* dominated pixels, including all four density classes, NDVI distributions varied with RS type (Fig. 8(a) and (b)). Median NDVI values for the RS$^-$ type were significantly lower than those of the non-RS type (p < 0.001; Wilcoxon rank-sum test) for both C-VV and C-VH σ°. C-VH σ° results showed a considerably larger number of RS$^-$ type pixels with a wider range of NDVI values than C-VV. NDVI results were consistent with the RS-type distributions: for C-VV σ°, only the "Sparse" class had a high RS$^-$ percentage, whereas, for C-VH σ°, all "Sparse", "Sparse & Medium", and "Medium" classes had high RS$^-$ type percentages (Table 4).

For the "Medium and Dense *Cladium*" class in S3A, the median NDVI value of the RS$^\pm$ type in C-VV σ° was significantly lower than that of the non-RS type (p < 0.001; Wilcoxon rank-sum) (Fig. 8(c)). The non-RS type was dominant in C-VH σ° results (Fig. 8(d)).

7. Discussion

This study investigated the role of water depth and vegetation density and morphology in spatiotemporal variations of Sentinel-1C-VV and C-VH backscatter at a 30-m resolution. Previous studies that relied on single-date SAR data needed to average several pixels to obtain the level of uncertainty for assessing backscatter variability as a function of surface characteristics. For example, the soil moisture monitoring study of Bourgeau-Chavez et al. (2007) used 200 × 200 m area (8 × 8 of 25 m pixels) to overcome uncertainties due to speckle noise. Our study clearly showed that Sentinel-1 SAR time series data were sufficient for detecting statistically significant σ°-d_w correlations at a 30 × 30 m resolution.

Here we interpret microwave scattering behavior in response to water depth (as a proxy for the height of vegetation above water surfaces) and vegetation types. First, we provide physical explanations for the temporal backscatter changes in the first three example pixels (Fig. 6) (Section 7.1). Second, we interpret the role of vegetation density and morphology in linear σ°-d_w relationships (Section 7.2). Third, we compare the vegetation characteristics and scattering behavior between this study and previous ones (Section 7.3). Fourth, we explain the positive correlations between backscatter and groundwater levels (Section 7.4). Finally, we discuss the limitations of this study (Section 7.5).

7.1. Changes in scattering mechanisms in response to water depth variations

Our results (Section 6.1, Fig. 6) indicated that significant linear relationships between C-band σ° and d_w, which were only detected from co-polarized observations in previous studies (Kasischke et al., 2003, 2009; Lang and Kasischke, 2008), also occurred in C-VH observations. Overall, our C-VV results for the linear relationships (Fig. 6(b), (f), and (j)) were similar to the previous studies (Section 2.2). This section provides physical explanations for the observed C-VV and C-VH σ°-d_w linear relationships based on changes in scattering mechanisms in response to varying water depths, according to the three vegetation types (Fig. 9).

The example of the "Shrubs & Trees" pixel in S3A showed a positive linear relationship between σ° and d_w for both C-VV and C-VH data (Fig. 6(b) and (d)). As water depth increases up to 125 cm (Fig. 6(a)), the volume of understory canopy decreases, which results in a two-way increase of microwave energy transmission because the incident microwave radiation has fewer obstacles in the canopy that absorb or scatter the energy in diffuse directions. As a result, there is more microwave energy to reflect from the water surface to interact with trunks and branches (enhanced double bounce and multiple-path scattering, respectively) before returning to the SAR (Fig. 9(a) - (c)). In addition, the reduction in canopy volume also increases the scattered microwave energy due to reduced canopy attenuation. The linear model for C-VH σ° and d_w had a shallower slope than C-VV, suggesting that C-VH σ° is less sensitive to changes in water depth because water depth rises mainly

enhance double-bounce scattering with limited depolarization (returning vertically polarized energy). A portion of double-bounce scattering (due to rotated dihedral of ground-trunk) and multiple-path scattering leads to the backscattered horizontally polarized energy (C-VH), but with less intensity than C-VV backscatter (Hong and Wdowinski, 2014). Stronger double-bounce components also result in higher C-VV σ° values than C-VH.

While the positive relationship is similar to the C-VV σ°-d_w linear relationship found by Lang and Kasischke (2008) in other forested wetlands, they attributed it to increase of the fraction of the water surface area as water depth rises due to micro-topography variations (Fig. 2 (a) - (c)). Though micro-topography could play an important role in backscatter increase under low-level flooded states (Lang and Kasischke, 2008), it can only partially explain backscatter changes in the very early stage of water depth increase. In our study area, micro-topography variations occur when rock outcroppings and solution holes increase the local variability of the ground surface. When soil fills in solution holes and evens out the irregular surfaces, the micro-topography is minimal. Micro-topography in herbaceous wetlands is very low because of a thick layer of peat soils that covers the rock underneath it. Micro-topography variations due to ground level variations are usually within 10 cm for the "Shrubs and Trees" in the S3A study area and a lot less than that in areas of "Medium and Dense *Cladium*" growing on thick layers of peat. In addition, in densely vegetated marsh communities, soil surfaces are rarely exposed because of alive and dead leaf matter and periphyton cover.

For "Shrubs & Trees" (bayhead forests and shrubland), dense understory results in significant energy attenuations. As water depth rises, the volume of the emergent understory vegetation decreases, reducing the microwave energy attenuations and increasing energy transmission. Therefore, we concluded that an increase in the degree of microwave energy transmission in response to water depth increase is the main reason for the observed backscatter increase, and the soil micro-topography effect on backscatter is very limited.

The second example, a "Medium & Dense *Cladium*" pixel in S3A, showed a combined positive and negative linear relationship between σ° and d_w for both C-VV and C-VH σ° (Fig. 6(f) and (h)). Similar to the first example, the increase of backscatter under shallow flooded states can also be attributed to the enhanced double-bounce and multiple-path scattering energy resulting from less canopy attenuation of the microwave energy in both incident and returning directions. C-VH σ° had less sensitivity (a shallower slope) to variations in water depths because of a weak double-bounce and multiple-path scattering component (Fig. 9 (g)). Under deep flooded states, the observed decrease of C-VV and C-VH backscatter as water depth increases is because the volume of vegetation available to interact with microwave energy decreases, resulting in reduced canopy scattering, double-bounce scattering, and multiple-path scattering (Fig. 9(h)). C-VH σ° (with a steeper slope) is more sensitive to water depth changes than C-VV σ°.

The third example, a "Sparse *Cladium*" pixel in NESRS, displayed a strong negative relationship between σ° and d_w for both C-VV and C-VH σ° (Fig. 6(j) and (l)). Increasing water depth reduces canopy backscatter and multiple-path scattering leading to the decrease of both C-VV and C-VH σ° (Fig. 9(k) - (m)). Similar to the second example under deep flooded states, C-VH σ° (with a steeper slope) is more sensitive to water depth than C-VV (Fig. 9(n) and (o)). Also, C-VH σ° had lower values than C-VV because of the limited energy depolarization generated by multiple-path and canopy scattering.

7.2. Vegetation characteristics effects on scattering behavior

We found considerable variations in RS-type distributions among the 20 major vegetation classes of varying densities and growth morphologies (Tables S4, S5). To understand the effect of vegetation density and morphology separately on scattering behavior represented by the RS types, we analyzed RS-type distributions within several selected

Table 10

Comparison of *Cladium* vegetation characteristics and scattering behavior between studies. "***" indicates no available dataset.

Study Area	Vegetation Class	Height (cm)	Biomass (g/m²)	C-VV RS type	C-VH RS type	Literature
NESRS	Sparse *Cladium*	165	246 ± 40	RS⁻	RS⁻	Sah et al. (2020); Kalla and Scheidt (2017)
	Sparse & Medium *Cladium*	175	246 ± 40	non-RS	RS⁻	
	Medium *Cladium*	189	246 ± 40	non-RS	RS⁻	
	Dense *Cladium*	216	246 ± 40	non-RS	non-RS	
S3A	Medium & Dense *Cladium*	202	352 ± 37	RS±	non-RS	
BCNP	Marl Prairie	44	330	RS⁻	***	Kasischke et al. (2003)
Alaskan wetlands	Non-forested Sites	48–70	***	RS⁻	***	Kasischke et al. (2009)

vegetation classes. First, we investigated the effect of density of the tall graminoid species *Cladium jamaicense*, which covered most of NESRS and the ridges of S3A (Fig. 3(b) and (c)). Second, we investigated the effect of vegetation morphology on scattering behavior for the five most abundant plant morphologies (Table 5, 7, 8).

7.2.1. Vegetation density effects on scattering behavior of Cladium

RS-type distributions for the five *Cladium* density classes suggest that density determines the ratio between RS⁻ and non-RS types' percentages for both polarizations (Table 4). Sparse classes had the highest RS⁻ type percentage in both polarizations, suggesting that backscatter from sparse *Cladium* is primarily canopy scattering (with little double-bounce scattering) that decreases as water depth increases (Fig. 9(k) - (m)), a result consistent with that of Pope et al. (1997) and Kasischke et al. (2003). Most of the pixels that were classified as RS⁻ type for both polarizations had steeper slopes in C-VH σ° than C-VV (e.g., Fig. 6(j) and (l)), suggesting that C-VH σ° is more sensitive to water depth changes. With increasing *Cladium* density, RS⁻ type percentage decreased for both polarizations because higher vegetation density results in less

transmission of microwave energy through the canopy and an increase of double-bounce scattering, especially for C-VV σ° (Supplementary Materials Fig. S6). For C-VH σ°, the slope became shallower as the density increased from sparse to medium dense (Table 6), indicating backscatter from sparse vegetation is the most sensitive to variations in water depths. NDVI value distribution of the RS⁻ type is much wider for C-VH σ° than C-VV (Fig. 8(a) and (b)), indicating a wider range of *Cladium* density is characterized by strong σ°-d_w correlations for C-VH σ°. Overall, for sparse to medium dense *Cladium*, C-VH σ° had greater sensitivity to water depth changes than C-VV σ°.

Cladium in S3A ("Medium & Dense *Cladium*" class) was denser than that in NESRS, as evidenced by the differences in their NDVI values (Fig. 8). The C-VV results indicated that nearly half of the pixels are RS± type (Table 4), and the Wilcoxon rank-sum statistical test showed that median NDVI for RS± was significantly lower than the non-RS type (Fig. 8(c)). Non-RS type occurred mainly in very dense *Cladium*, most likely because of low microwave energy transmission through the canopy.
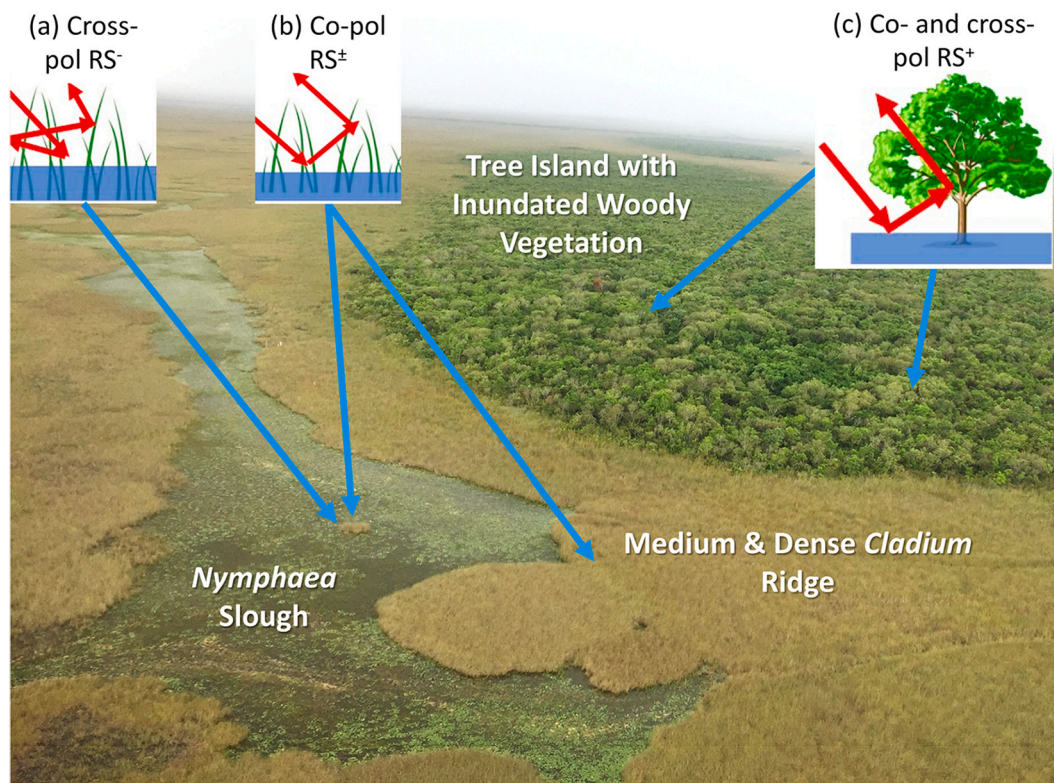

Fig. 10. Aerial photograph of ridge and slough landscape with various scattering behavior. The ridges are covered with mixed medium and dense *Cladium*, and the sloughs are characterized by floating broadleaf *Nymphaea*, submerged and floating periphyton, and *Cladium* marshes. (a, b, c) three vegetation types (indicated by the text in white) as possible RS types in C-VV or C-VH σ°. (a) "Floating/Submerged & Tall Graminoid" morphology as the RS⁻ type in C-VH σ°. (b) "Medium & Dense" *Cladium* in ridges and "Floating/Submerged & Tall Graminoid" morphology in sloughs as the RS± type in C-VV σ°. (c) Inundated woody vegetation located on tree islands as the RS⁺ type in both C-VV and C-VH σ°. Note that the non-RS type is not shown here, which accounts for considerable areas in the ridge and slough landscape.

7.2.2. Vegetation morphology effects on scattering behavior

We analyzed RS-type distributions for five vegetation growth morphologies: "Tall Graminoid", "Short Graminoid", "Floating/Submerged & Tall Graminoid", "Woody", and "Broadleaf Emergent" vegetation.

Comparing the three sparse density graminoid classes in NESRS: *Cladium*, "Graminoid Prairie" (including species such as *Muhlenbergia capillaris*), and "Graminoid Marsh" (including species such as *Eleocharis* spp., *Rhynchospora* spp., *Panicum* spp.) (Table 5), revealed that tall graminoids had higher RS$^-$ type percentages than short graminoids in both polarizations. Considering short graminoid species, the median pixel-based maxima of water depth was 61 cm, and the maximum was 95 cm, which submerged large portions of many short graminoids for long periods resulting in backscatter insensitivity to water depth changes. However, backscatter from the tall graminoid is constantly sensitive to water depth changes because a significant volume of the plants is above the water surface at all times (e.g., *Cladium* heights are over 160 cm according to Table 10). Therefore, plant height indicates the water depth range, to which SAR backscatter can be sensitive. Also, "Graminoid Prairie" had the steepest slope values for both C-VV and C-VH σ°, indicating high sensitivity of backscatter in response to changes in water depth.

S3A slough were characterized by three "Floating/Submerged & Tall Graminoid" vegetation classes (Table 8). For the class "Broadleaf Floating & Submerged", the presence of the emergent species *Cladium* among floating and submerged species in a slough environment was much lower (~4% on average) than for the other two classes. The three classes had different scattering behavior in C-VV σ°, but similar behavior in C-VH σ°. For C-VV, RS$^\pm$ did not exist in the "Broadleaf Floating & Submerged" class, but it occurred in the "*Nymphaea & Cladium*" and "*Periphyton & Cladium*" classes, because the emergent *Cladium* is dense enough to induce double-bounce scattering within the floating vegetation matrix (Fig. 10(b)). However, for C-VH σ°, the RS$^-$ type occurred for all three classes with similar slope values (Table 9), indicating similar backscatter sensitivity to water depth variations. The non-RS type was dominant for both C-VV and C-VH σ°. Overall, the ridge and slough landscape can provide all three RS types (RS$^+$, RS$^\pm$, RS$^-$) in both C-VV and C-VH data (Fig. 10).

Woody vegetation RS-type distributions differed between the two study areas (Table 7). Woody vegetation in NESRS was dominated by the non-RS type, most likely because they were either located at elevated ground surfaces or tree islands that were rarely inundated. The halo-shaped forests around culverts along Tamiami Trail (deep and light green fringes at the northern edge of Fig. 3(b)) were classified into the non-RS type (Fig. 7(a)), despite low elevation and long hydroperiods, because dense tree canopies of *Annona glabra* and dense, tall understory broadleaf vegetation (e.g., ferns) can reduce the transmission of microwave energy. In contrast, woody vegetation in S3A, mostly located on lower elevation parts of the tree islands (tails) where bayhead forests and shrubs dominate (Fig. 10(c)), had many RS$^+$ type pixels in C-VV σ° and fewer RS$^+$ type pixels in C-VH σ°. RS$^+$ type pixels are attributed to deep water depths throughout the year, with remarkable water depth variations greater than 1 m. However, the northern part of large tree islands (heads) is elevated and rarely inundated, thus showing non-RS type behavior (e.g., the southeastern corner tree island in Fig. 3(c), Fig. 7(c)). Similarly, the broadleaf emergent species also showed considerable RS$^+$ type pixels for both C-VV and C-VH σ° because their tall emergent stems functioned as corner reflectors to induce double-bounce scattering. The S3A woody and broadleaf emergent morphology vegetation types were characterized by shallow slopes (0.04 dB/cm) for both polarizations (Table 9), indicating that the backscatter is less sensitive to water depth changes compared to the herbaceous vegetation in NESRS.

In contrast to the positive σ°-d$_w$ correlation for forested wetlands found in this study, Kasischke et al. (2003) found negative correlations for cypress/pines sites in the Everglades BCNP. Different types of correlations could be attributed to biophysical parameters of trees, which play essential roles in C-band microwave energy interaction with forest layers (Fig. 1). For our study, the positive σ°-d$_w$ correlations in both C-VV and C-VH are attributed to trees about 5–10 m high with some open canopy that allows the double-bounce and multiple-path scattering to return to the SAR. The cypress/pine vegetation in Kasischke et al. (2003) has different physical characteristics from our bayhead swamp forest and shrubland. More field surveys are required to understand this difference in scattering behavior for the different forest and shrubland types. However, both studies are consistent in C-band backscatter being more sensitive to variations in water depths for herbaceous than woody vegetation.

7.3. Comparison of vegetation characteristics of key wetland types

We compared the NESRS and S3A *Cladium jamaicense* vegetation height and biomass with the herbaceous vegetation characteristics from another two studies that discovered RS$^-$ type backscatter behavior using ERS SAR C-VV data (Table 10, Kasischke et al., 2003, 2009). For the *Cladium* vegetation in NESRS, as the density increases from "Sparse" to "Dense" class, *Cladium* mean height increases from 165 to 216 cm. *Cladium* in WCA-3A has higher vegetation biomass than those in ENP. Sparse *Cladium* in NESRS is predominantly RS$^-$ type, whereas medium and dense *Cladium* in S3A is predominantly RS$^\pm$ type. In comparison, according to Kasischke et al. (2003), marl prairies in BCNP, with shorter stature but a higher level of biomass than the "Sparse *Cladium*" class in NESRS, had significant negative σ°-d$_w$ relationships but weaker σ°-d$_w$ correlations (an average R^2 value of 0.18). The Alaskan marsh wetlands with taller emergent vegetation than BCNP marl prairies also behaved as the RS$^-$ type with stronger σ°-d$_w$ correlations (an average R^2 value of 0.67). This comparison analysis reveals that backscatter from taller and less dense herbaceous vegetation is more sensitive to changes in water depths with a negative correlation.

7.4. Backscatter variations during unflooded periods in NESRS

We detected many unflooded RS$^+$ type pixels in NESRS with significant positive σ°-d$_w$ correlations. Similar positive correlations were also detected by J.-W. Kim et al. (2017b), who found three-way positive correlations between backscatter (in both C- and L-band), groundwater levels, and soil moisture. Bechtold et al. (2018) found positive correlations between C-VV backscatter with groundwater levels in peatlands, and they attributed it to backscatter's sensitivity to variation in soil moistures. Kasischke et al. (2003) found a strong, positive correlation between C-VV backscatter and soil moisture in the Everglades. However, for most NESRS, the soil surface is often covered by deposits of dead plant matter, debris, and periphyton mats. We suggest that the detected unflooded RS$^+$ type can be attributed to variations in the moisture of those ground-cover materials or the soil moisture, depending on the degree of transmission of the C-band microwave energy. High groundwater levels lead to high moisture and enhancement of backscatter.

Unflooded RS$^+$ type occurred in both C-VV and C-VH σ° for all vegetation types in NESRS. C-VV σ° results showed a much higher unflooded RS$^+$ type percentage (Table S5 and Fig. S7) than C-VH because C-VV σ° includes a stronger diffuse scattering component (Fig. 1) that is related to soil moisture (Kasischke and Bourgeau-Chavez, 1997). Woody vegetation showed a low unflooded RS$^+$ type percentage in C-VV (less than 5%) and negligible percentages in C-VH σ° because canopy attenuates microwave energy. Herbaceous vegetation showed high unflooded RS$^+$ type percentages regardless of densities. For example, all four density classes of *Cladium* displayed significant unflooded RS$^+$ type percentages. The results indicate that a significant proportion of C-band microwave energy can be transmitted through *Cladium* canopies to reach soil surfaces. A high level of soil/ground-cover materials moisture leads to enhanced double-bounce and multiple-path scattering and, therefore, higher backscatter (Fig. 1(b), Kasischke and Bourgeau-Chavez (1997)).

7.5. Limitations and future work

Our study's main limitations arose from the low accuracy of the two DTMs used to analyze the relationships between σ° and d_w. NESRS used a LiDAR DTM with high horizontal resolution (0.5 m) but only a moderate vertical accuracy of 34.8 cm, which in most cases overestimated ground elevations due to dense vegetation (Dewberry, 2018) and consequently underestimated water depth. Thus, DTM errors affected RS-type classification, which did not use negative water depth values. The S3A DTM product was characterized by a coarser grid (400 m × 400 m), which did not account for small-scale topographic features and, therefore, also affected the RS-type classification by smoothing across varying water depths in heterogeneous vegetation types within a single grid cell.

Other limitations arose from the spatial resolution of the 30-m grid. The 30-m scale vegetation class indicating representative vegetation type(s) enabled us to discover different scattering behavior for various vegetation types. However, minor vegetation types existing within individual grid cells may affect scattering behavior and NDVI values that were not resolved in this analysis. To increase confidence in the interpretation of scattering patterns for different vegetation types requires higher-resolution (meter level) SAR data or exclusion of more heterogeneous vegetation patches.

Sensitivity test on n_{th} values from 2 to 20 (representing 3% to 30% of scenes in the SAR time series) had a limited impact on RS-type percentages (Table S2). We suggest that n_{th} of 7 (10%) best represents σ°-d_w scatter plots and leads to accurate RS classification (discussion in Supplementary Material Note 3). The time span of SAR data can also impact RS-type classification results. The sensitivity study indicates that three years is the minimum length to reflect the backscatter behavior versus water depths. A shorter time span led to high variability in RS-type classification (Table S3) because water depth ranges varied among years. For example, S3A showed significant differences (44.8%) when only using the first year (2016 April - 2017 April) of C-VV data because many pixels were classified as the RS$^+$ type, and most of these pixels were reclassified as RS$^\pm$ type when using three-year data. Since the first year was characterized by shallower water depths than the second year (e.g., Fig. 6(e)), σ° and d_w were positively correlated, and they were reclassified as the RS$^\pm$ type when involving more data under deeper flooded states. However, for C-VH σ°, the second-year results showed the most significant difference (40.9%) because many pixels were classified as the RS$^-$ type, whereas they were reclassified as the non-RS type when involving more data under shallower flooded states. Consequently, we suggest a three-year minimum time series to achieve significant water depth variations and actual RS-type classification.

This study focused on C-band wavelength, whereas RS-type classification using L-band wavelength data could lead to different results for the investigated vegetation types. For woody vegetation, RS$^+$ type pixels with more sensitive backscatter to water depth changes are expected because L-band energy is characterized by a higher degree of transmission through canopies than C-band. For dense herbaceous vegetation, some C-VV RS$^\pm$ type pixels may be reclassified as RS$^-$ in L-band data because producing double-bounce scattering in L-band microwave energy needs a higher vegetation density than in the C-band (Pope et al., 1997). J.-W. Kim et al. (2014) correlated ALOS PALSAR L-HH observations and water level data measured in Everglades herbaceous sites and found most of the sites with negative σ°-d_w correlations (RS$^-$ type) and no sites with a combination of positive and negative correlations (RS$^\pm$ type). Their negative slope values of L-HH σ°-d_w correlations are similar to our study (Table 6). Some C-band non-RS type pixels (e.g., *Typha*) may be reclassified as the RS$^\pm$ type because more L-band microwave energy can be transmitted through vegetation canopy. Sparse herbaceous vegetation that was classified as RS$^-$ type in C-VV and C-VH σ° may also have strong negative σ°-d_w correlations for the L-band data (both co- and cross-polarization) based on Pope et al. (1997).

Future studies could conduct similar studies in other wetlands under the condition of available DTMs and accurate water surfaces interpolated by measurements from a dense network of water gauges. Future work can use SAR backscatter to estimate water depth changes in wetlands. J.-W. Kim et al. (2014) successfully used σ° to estimate changes in water depth, whereas the estimation was limited to point locations of water gauges, and no vegetation information was taken into account. Our study demonstrates the possibility of water depth change mapping by selecting the three RS types using vegetation density and growth morphology as criteria. Future works can apply the slopes of σ°-d_w linear relationships calculated in this study on different vegetation types to estimate regional water depth changes. For wetlands with short hydroperiods, future studies can investigate the relationship among SAR backscatter, groundwater, and soil moisture data (e.g., Soil Moisture Active Passive (SMAP)). Future studies could also use other wavelengths of SAR data (e.g., L- and S-band from NISAR (NASA-ISRO SAR) Mission) for a similar type of research.

8. Conclusions

Our study showed that C-VV and C-VH backscatter were sensitive to water depth changes in large areas of the Everglades wetlands. Pixels showing consistent linear relationships were termed reliable scatterers (RS) and classified based on the σ°-d_w linear relationships as RS$^+$ (positive), RS$^\pm$ (positive-negative), RS$^-$ (negative), and non-RS (weak relationships) types. To our knowledge, it is the first study that found a strong correlation between C-VH σ° and d_w.

The observed σ°-d_w linear relationships were interpreted with changes in scattering mechanism in response to water depth changes representing microwave energy-water-vegetation interactions. Such interactions significantly varied with vegetation type, demonstrated by woody vegetation, mixed medium and dense *Cladium*, and sparse *Cladium* vegetation examples. C-VV and C-VH backscatter were similar in linear relationship types but different in sensitivity and strength of correlation to variations in water depths according to vegetation types.

Vegetation density and morphology had a significant impact on RS types. Both C-VV and C-VH backscatter were the most sensitive to water depth changes for sparse herbaceous vegetation, and this sensitivity decreased as vegetation density increased. For sparse to medium dense *Cladium*, RS$^-$ was the dominant RS type for C-VH σ°. However, for mixed medium and dense *Cladium*, RS$^\pm$ was the dominant RS type for C-VV σ°. Ridge and slough landscape vegetation can serve as three RS types (RS$^+$, RS$^\pm$, RS$^-$) for C-VV or C-VH σ°.

Large areas in NESRS were classified as the unflooded RS$^+$ type using C-VV data, indicating a strong positive correlation between groundwater levels and backscatter. We suggest that groundwater level variations could influence the moisture of soil or ground-cover materials, leading to backscatter variations.

Overall, this comprehensive study provides insights into the role of water depth (surface water and groundwater) and vegetation characteristics in spatiotemporal variations of Sentinel-1 dual-polarization SAR backscatter. This study serves as a conceptual basis for future studies on monitoring wetlands' hydrologic patterns and interpretations of SAR backscatter observations.

Declaration of Competing Interest

The authors declare that they have no known competing financial interests or personal relationships that could have appeared to influence the work reported in this paper.

Acknowledgements

Appendix A. Supplementary data

Supplementary data to this article can be found online at https://doi.org/10.1016/j.rse.2021.112864.

References

Bechtold, M., Schlaffer, S., Tiemeyer, B., De Lannoy, G., 2018. Inferring water table depth dynamics from ENVISAT-ASAR C-band backscatter over a range of peatlands from deeply-drained to natural conditions. Remote Sens. 10, 536. https://doi.org/10.3390/rs10040536.
Beget, M.E., Di Bella, C.M., 2007. Flooding: the effect of water depth on the spectral response of grass canopies. J. Hydrol. 335, 285–294. https://doi.org/10.1016/j.jhydrol.2006.11.018.
Bourgeau-Chavez, L.L., Smith, K.B., Brunzell, S.M., Kasischke, E.S., Romanowicz, E.A., Richardson, C.J., 2005. Remote monitoring of regional inundation patterns and hydroperiod in the Greater Everglades using synthetic aperture radar. Wetlands 25, 176. https://doi.org/10.1672/0277-5212(2005)025[0176:RMORIP]2.0.CO;2.
Bourgeau-Chavez, L.L., Kasischke, E.S., Riordan, K., Brunzell, S., Nolan, M., Hyer, E., Slawski, J., Medvecz, M., Walters, T., Ames, S., 2007. Remote monitoring of spatial and temporal surface soil moisture in fire disturbed boreal forest ecosystems with ERS SAR imagery. Int. J. Remote Sens. 28, 2133–2162. https://doi.org/10.1080/01431160600976061.
Brisco, B., 2015. Mapping and monitoring surface water and wetlands with synthetic aperture radar. In: Tiner, R.W., Lang, M.W., Klemas, V.V. (Eds.), Remote Sensing of Wetlands: Applications and Advances. CRC Press, pp. 119–136.
Brisco, B., Schmitt, A., Murnaghan, K., Kaya, S., Roth, A., 2013. SAR Polarimetric Change Detection for Flooded Vegetation (null 6), pp. 103–114.
David, P.G., 1996. Changes in plant communities relative to hydrologic conditions in the Florida Everglades. Wetlands 16, 15–23. https://doi.org/10.1007/BF03160642.
Dewberry, 2018. Florida Everglades National Park Lidar. Topobathy Bare Earth DEM. https://doi.org/10.3390/s18030829.
Dobson, M.C., Ulaby, F.T., Pierce, L.E., Sharik, T.L., Bergen, K.M., Kellndorfer, J., Kendra, J.R., Li, E., Lin, Y.-C., Nashashibi, A., et al., 1995. Estimation of forest biophysical characteristics in northern Michigan with SIR-C/X-SAR. IEEE Trans. Geosci. Remote Sens. 33, 877–895. https://doi.org/10.1109/36.406674.
Filipponi, F., 2019. Sentinel-1 GRD preprocessing workflow. In: Multidisciplinary Digital Publishing Institute Proceedings, Vol. 18, No. 1, p. 11.
Fung, A.K., Ulaby, F.T., 1983. Matter-energy interaction in the microwave region. Manual Remote Sens. 1, 115–164.
Gamon, J.A., Field, C.B., Goulden, M.L., Griffin, K.L., Hartley, A.E., Joel, G., Penuelas, J., Valentini, R., 1995. Relationships between NDVI, canopy structure, and photosynthesis in three Californian vegetation types. Ecol. Appl. https://doi.org/10.2307/1942049.
Gann, D., 2018. Quantitative Spatial Upscaling of Categorical Data in the Context of Landscape Ecology: A New Scaling Algorithm. https://digitalcommons.fiu.edu/etd/3641.
Gann, D., 2019. Quantitative spatial upscaling of categorical information: the multi-dimensional grid-point scaling algorithm. Methods Ecol. Evol. 10, 2090–2104. https://doi.org/10.1111/2041-210X.13301.
Gann, D., Richards, J.H., Harris, B., 2019. Vegetation Change along Everglades National Park Boundary Areas of Northeast Shark River Slough, Between 2010/13 and 2016/17. Everglades National Park. https://digitalcommons.fiu.edu/gis/84/.
Gasparri, N.I., Parmuchi, M.G., Bono, J., Karszenbaum, H., Montenegro, C.L., 2010. Assessing multi-temporal Landsat 7 ETM+ images for estimating above-ground biomass in subtropical dry forests of Argentina. J. Arid Environ. 74, 1262–1270. https://doi.org/10.1016/j.jaridenv.2010.04.007.
Gitelson, A.A., 2004. Wide dynamic range vegetation index for remote quantification of biophysical characteristics of vegetation. J. Plant Physiol. 161, 165–173. https://doi.org/10.1078/0176-1617-01176.
Goldstein, R.M., Engelhardt, H., Kamb, B., Frolich, R.M., 1993. Satellite radar interferometry for monitoring ice sheet motion: application to an antarctic ice stream. Science 262, 1525–1530. https://doi.org/10.1126/science.262.5139.1525.
Grimaldi, S., Xu, J., Li, Y., Pauwels, V.R.N., Walker, J.P., 2020. Flood mapping under vegetation using single SAR acquisitions. Remote Sens. Environ. 237, 111582 https://doi.org/10.1016/j.rse.2019.111582.
Gunderson, L.H., 1994. Vegetation of the Everglades: Determinants of community composition. In: Everglades: The Ecosystem and its Restoration 323.
Han, L., Rundquist, D.C., 2003. The spectral responses of Ceratophyllum demersum at varying depths in an experimental tank. Int. J. Remote Sens. 24, 859–864.
Harvey, R.G., Loftus, W.F., Rehage, J.S., Mazzotti, F.J., 2011. Effects of Canals and Levees on Everglades Ecosystems: Circular. WEC304. IFAS Extension. University of Florida, Gainesville, FL, p. 21.
Heffernan, J.B., Ross, M.S., Cohen, M.J., Osborne, T.Z., Sah, J.P., Ruiz, P.L., Scinto, L.J., 2009. The Monitoring and Assessment Plan (MAP) Greater Everglades Wetlands Module- Landscape Pattern- Ridge, Slough, and Tree Island Mosaics: Year 1 Annual Report. SERC Research Reports.
Hong, S., Wdowinski, S., 2011. Evaluation of the quad-polarimetric Radarsat-2 observations for the wetland InSAR application. Can. J. Remote. Sens. 37, 484–492. https://doi.org/10.5589/m11-058.
Hong, S., Wdowinski, S., 2014. Double-bounce component in cross-Polarimetric SAR from a new scattering target decomposition. IEEE Trans. Geosci. Remote Sens. 52, 3039–3051. https://doi.org/10.1109/TGRS.2013.2268853.
Hong, S.H., Wdowinski, S., Kim, S.W., 2009. Evaluation of TerraSAR-X observations for wetland InSAR application. IEEE Trans. Geosci. Remote Sens. 48 (2), 864–873.
Inglada, J., Vincent, A., Arias, M., Marais-Sicre, C., 2016. Improved early crop type identification by joint use of high temporal resolution SAR and optical image time series. Remote Sens. 8, 362. https://doi.org/10.3390/rs8050362.
Johnston, K., Ver Hoef, J.M., Krivoruchko, K., Lucas, N., 2004. Using ArcGIS Geostatistical Analyst. Esri Redlands.
Jones, J.W., Price, S.D., 2007a. Conceptual Design of the Everglades Depth Estimation Network (EDEN) Grid. Geological Survey (US).
Jones, J.W., Price, S.D., 2007b. Initial Everglades Depth Estimation Network (EDEN) Digital Elevation Model Research and Development. Geological Survey (US).
Kalla, P.I., Scheidt, D.J., 2017. Everglades Ecosystem Assessment–Phase IV, 2014: Data Reduction and Initial Synthesis. United States Environmental Protection Agency, Science and Ecosystem Support Division, Athens, GA, p. 58 (SESD Project 14–0380).
Kasischke, E.S., Bourgeau-Chavez, L.L., 1997. Monitoring South Florida wetlands using ERS-1 SAR imagery. Photogramm. Eng. Remote. Sens. 63, 281–291.
Kasischke, E.S., Smith, K.B., Bourgeau-Chavez, L.L., Romanowicz, E.A., Brunzell, S., Richardson, C.J., 2003. Effects of seasonal hydrologic patterns in South Florida wetlands on radar backscatter measured from ERS-2 SAR imagery. Remote Sens. Environ. 88, 423–441. https://doi.org/10.1016/j.rse.2003.08.016.
Kasischke, E.S., Bourgeau-Chavez, L.L., Johnstone, J.F., 2007. Assessing spatial and temporal variations in surface soil moisture in fire-disturbed black spruce forests in interior Alaska using spaceborne synthetic aperture radar imagery — implications for post-fire tree recruitment. Remote Sens. Environ. https://doi.org/10.1016/j.rse.2006.10.020.
Kasischke, E.S., Bourgeau-Chavez, L.L., Rober, A.R., Wyatt, K.H., Waddington, J.M., Turetsky, M.R., 2009. Effects of soil moisture and water depth on ERS SAR backscatter measurements from an Alaskan wetland complex. Remote Sens. Environ. 113, 1868–1873. https://doi.org/10.1016/j.rse.2009.04.006.
Kim, D., Lee, H., Laraque, A., Tshimanga, R.M., Yuan, T., Jung, H.C., Beighley, E., Chang, C.-H., 2017a. Mapping spatio-temporal water level variations over the Central Congo River using PALSAR ScanSAR and Envisat altimetry data. Int. J. Remote Sens. 38, 7021–7040.
Kim, J.-W., Lu, Z., Jones, J.W., Shum, C.K., Lee, H., Jia, Y., 2014. Monitoring Everglades freshwater marsh water level using L-band synthetic aperture radar backscatter. Remote Sens. 150, 66–81. https://doi.org/10.1016/j.rse.2014.03.031.
Kim, J.-W., Lu, Z., Gutenberg, L., Zhu, Z., 2017b. Characterizing hydrologic changes of the great dismal swamp using SAR/InSAR. Remote Sens. Environ. https://doi.org/10.1016/j.rse.2017.06.009.
Lang, M.W., Kasischke, E.S., 2008. Using C-band synthetic aperture radar data to monitor forested wetland hydrology in Maryland's coastal plain, USA. IEEE Trans. Geosci. Remote Sens. 46, 535–546. https://doi.org/10.1109/TGRS.2007.909950.
Lang, M.W., Townsend, P.A., Kasischke, E.S., 2008. Influence of incidence angle on detecting flooded forests using C-HH synthetic aperture radar data. Remote Sens. Environ. 112, 3898–3907. https://doi.org/10.1016/j.rse.2008.06.013.

Le Toan, T., Ribbes, F., Wang, Li-Fang, Floury, N., Ding, Kung-Hau, Kong, Jin Au, Fujita, M., Kurosu, T., 1997. Rice crop mapping and monitoring using ERS-1 data based on experiment and modeling results. IEEE Trans. Geosci. Remote Sens. 35, 41–56. https://doi.org/10.1109/36.551933.

Liao, H., Wdowinski, S., Li, S., 2020. Regional-scale hydrological monitoring of wetlands with Sentinel-1 InSAR observations: case study of the South Florida Everglades. Remote. Sens. Environ. 251, 112051.

Liu, Z., Volin, J.C., Dianne Owen, V., Pearlstine, L.G., Allen, J.R., Mazzotti, F.J., Higer, A. L., 2009. Validation and ecosystem applications of the EDEN water-surface model for the Florida Everglades. Ecohydrology: ecosystems, land and water process interactions. Ecohydrogeomorphology 2, 182–194.

Malone, Sparkle., 2019. Fire perimeter files for wild and prescribed fires in Everglades National Park 1948-2019. Knowledge Network for Biocomplexity urn:uuid: 8f4ef485-6f2a-44ca-8c6f-9766b59ad098.

Palaseanu, M., Pearlstine, L., 2008. Estimation of water surface elevations for the Everglades, Florida. Comput. Geosci. 34, 815–826. https://doi.org/10.1016/j.cageo.2007.08.004.

Pope, K.O., Rejmankova, E., Paris, J.F., Woodruff, R., 1997. Detecting seasonal flooding cycles in marshes of the Yucatan peninsula with SIR-C polarimetric radar imagery. Remote Sens. Environ. https://doi.org/10.1016/s0034-4257(96)00151-4.

Pulvirenti, L., Chini, M., Pierdicca, N., Guerriero, L., Ferrazzoli, P., 2011. Flood monitoring using multi-temporal COSMO-SkyMed data: image segmentation and signature interpretation. Remote Sens. Environ. 115, 990–1002. https://doi.org/10.1016/j.rse.2010.12.002.

Pulvirenti, L., Pierdicca, N., Chini, M., Guerriero, L., 2013. Monitoring flood evolution in vegetated areas using cosmo-skymed data: the tuscany 2009 case study. IEEE J. Selec. Top. Appl. Earth Observ. Remote. 6, 1807–1816. https://doi.org/10.1109/jstars.2012.2219509.

Puri, S., Stephen, H., Ahmad, S., 2011. Relating TRMM precipitation radar backscatter to water stage in wetlands. J. Hydrol. 401, 240–249. https://doi.org/10.1016/j.jhydrol.2011.02.026.

Ramsey, E.W., 1995. Monitoring flooding in coastal wetlands by using radar imagery and ground-based measurements. Int. J. Remote Sens. 16, 2495–2502.

Ross, M.S., Heffernan, J.B., Sah, J.P., Isherwood, E., Blanco, J., 2016. Everglades Ridge, Slough, and Tree Island Mosaics. Annual Report submitted to US Army Engineer Research and Development Center. Cooperative Agreement #: W912HZ-10-2-0030. Modification # P00004. Year 5 Report (2010-2015): Feb 2016, 98 pp.

Sah, J.P., Heffernan, J.B., Ross, M.S., Isherwood, E., Castrillon, K., 2020. Landscape Pattern- Ridge, Slough, and Tree Island Mosaics. Annual Report – Year 4 (2015-2019) submitted to US Army Engineer Research and Development Center, 56 pp.

Steward, K.K., Ornes, W.H., 1975. The autecology of sawgrass in the Florida Everglades. Ecology 56 (1), 162–171. https://doi.org/10.2307/1935308.

Townsend, P.A., 2001. Mapping seasonal flooding in forested wetlands using multi-temporal Radarsat SAR. Photogramm. Eng. Remote. Sens. 67, 857–864.

Townsend, P.A., 2002. Relationships between forest structure and the detection of flood inundation in forested wetlands using C-band SAR. Int. J. Remote Sens. 23, 443–460.

Tsyganskaya, V., Martinis, S., Marzahn, P., Ludwig, R., 2018. Detection of temporary flooded vegetation using Sentinel-1 time series data. Remote Sens. 10, 1286. https://doi.org/10.3390/rs10081286.

Vermote, E., Justice, C., Claverie, M., Franch, B., 2016. Preliminary analysis of the performance of the Landsat 8/OLI land surface reflectance product. Remote Sens. Environ. 185, 46–56. https://doi.org/10.1016/j.rse.2016.04.008.

Wang, Y., Kasischke, E.S., Melack, J.M., Davis, F.W., Christensen, N.L., 1994. The effects of changes in loblolly pine biomass and soil moisture on ERS-1 SAR backscatter. Remote Sens. Environ. 49, 25–31. https://doi.org/10.1016/0034-4257(94)90056-6.

Wang, Y., Davis, F.W., Melack, J.M., Kasischke, E.S., Christensen, N.L., 1995. The effects of changes in forest biomass on radar backscatter from tree canopies. Int. J. Remote Sens. 16, 503–513.

Watts, D.L., Cohen, M.J., Heffernan, J.B., Osborne, T.Z., 2010. Hydrologic modification and the loss of self-organized patterning in the ridge–slough mosaic of the Everglades. Ecosystems 13, 813–827. https://doi.org/10.1007/s10021-010-9356-z.

Wdowinski, S., Hong, S.H., 2015. Wetland InSAR: a review of the technique and applications. Remote Sens. Wetlands: Appl. Adv. 137–154.

Yuan, T., Lee, H., Jung, H.C., 2015. Toward estimating wetland water level changes based on hydrological sensitivity analysis of PALSAR backscattering coefficients over different vegetation fields. Remote Sens. 7, 3153–3183. https://doi.org/10.3390/rs70303153.

Zhang, B., Wdowinski, S., Oliver-Cabrera, T., Koirala, R., Jo, M., Osmanoglu, B., 2018. Mapping the extent and magnitude of sever flooding induced by hurricane IRMA with multi-temporal SENTINEL-1 SAR and Insar observations. Int. Arch. e Photogramm. Remote Sens. Spatial Inf. Sci 42, 2237–2244.

Zhang, M., Li, Z., Tian, B., Zhou, J., Tang, P., 2016. The backscattering characteristics of wetland vegetation and water-level changes detection using multi-mode SAR: a case study. Int. J. Appl. Earth Obs. Geoinf. 45, 1–13. https://doi.org/10.1016/j.jag.2015.10.001.